

ISSET JOURNAL OF EARTHQUAKE TECHNOLOGY

Vol. 48

No. 2-4

June-December 2011

CONTENTS

No.	Paper	Page
516	Liquefaction Potential of Sabarmati-River Sand S.V. Dinesh, G. Mahesh Kumar, Muttana S. Balreddy and B.C. Swamy	61
517	Neural-Network Based Estimation of Normalized Response Spectra C.R. Arjun and Ashok Kumar	73
	Technical Note	
	Effectiveness of Multiple TSWDs for Seismic Response Control of Masonry- Infilled RC Framed Structures Nishant Kishore Rai, G.R. Reddy and V. Venkatraj	85

Financial Assistance from AICTE and DST, New Delhi for the Publication of ISET Journals for 2011–2012 is duly acknowledged.

LIQUEFACTION POTENTIAL OF SABARMATI-RIVER SAND

S.V. Dinesh*, G. Mahesh Kumar*, Muttana S. Balreddy* and B.C. Swamy**

*Department of Civil Engineering
Siddaganga Institute of Technology, Tumkur-572103

**Department of Civil Engineering
Central Connecticut State University, New Britain, CT 06053, U.S.A.

ABSTRACT

Liquefaction of saturated sandy soils has been studied by several researchers and liquefaction potential depends on initial confining pressure, relative density, amplitude of cyclic stress, etc. The Bhuj earthquake caused extensive damage in several parts of Gujarat. In the present paper, the results of stress-controlled cyclic triaxial tests on soil samples obtained from the Sabarmati river-bed in the Ahmedabad city, Gujarat are reported for various relative densities at the 100-kPa confining pressure. The results of cyclic strength, excess pore water pressure development and dynamic properties are analyzed. The liquefaction resistance is qualitatively compared to that of the Toyoura sand. It is found that liquefaction strength increases with relative density and correlates well with the normalized shear strength obtained from the consolidated undrained tests.

KEYWORDS: Liquefaction, Pore Pressure Ratio, Cyclic Resistance Ratio, Shear Modulus

INTRODUCTION

Liquefaction is a phenomenon that leads to the complete loss of shear strength due to the development of excess pore water pressure. During the earthquakes, saturated sandy deposits undergo liquefaction. Generally, there will be a complete loss of strength or development of excessive strains. Liquefaction gained importance after the Niigata and Alaska earthquakes of 1964. There has been a lot of research in these years, and significant contributions have been made and state-of-the-art papers have been published to understand the concept (Lee and Seed, 1967; Ishihara et al., 1975; Ishihara, 1985; Li et al., 1988; Ishihara, 1993; Hyodo et al., 1998; Polito and Martin II, 2001; Baxter et al., 2008).

The liquefaction resistance is generally evaluated either by laboratory or field methods. In the laboratory method cyclic triaxial and simple shear tests are widely used on reconstituted or undisturbed soil samples. Liquefaction is a strain-softening type of undrained response involving excessive deformations. The liquefaction or cyclic softening is defined in terms of cyclic stress ratio to produce 5% double-amplitude axial strain or 100% excess pore water pressure development (i.e., zero deviator stress) in 20 cycles of uniform load application. This cyclic stress ratio is also called as cyclic resistance ratio (CRR), synonymous with the 'cyclic strength'.

In view of the difficulty in obtaining undisturbed soil samples, the liquefaction strength is obtained by using reconstituted soil samples. The liquefaction resistance of saturated reconstituted sands in laboratory has been studied extensively by several researchers (Seed, 1979; Finn, 1981; Govindaraju, 2005; Ravishankar, 2006), and it has been concluded that initial confining stress, cyclic shear stress and void ratio affect the liquefaction resistance. Tatsuoka et al. (1986) have shown for the Toyoura sand that CRR increases linearly with relative density up to 70%, and thereafter, CRR increases rapidly with an increase in relative density.

The Bhuj earthquake in 2001 caused extensive loss of life and damage to the infrastructure in Gujarat, India. There were wide-spread sand boils and liquefaction. Bhandari and Sharma (2001) have observed a pattern of damage in the Ahmedabad city, in which a number of damaged multistoried buildings were scattered on the left and right banks of the Sabarmati river. The damage was more around the Sabarmati river-bed, which consists of unconsolidated sediments of recent origin. In this connection, it has been felt necessary to establish liquefaction criteria for the unconsolidated sediments of the Sabarmati river-bed. Stress-controlled cyclic triaxial tests are conducted on sand sediments obtained from the Sabarmati river-bed and an attempt is made to qualitatively compare the current results with those of the Japanese Toyoura sand.

MATERIALS AND EXPERIMENTAL METHODS

1. Physical Properties of Materials

In the present investigation sand samples are obtained from the Sabarmati river-bed in the Ahmedabad city for characterizing the liquefaction potential. The sand samples are collected from a depth of 3 m from the excavated pits close to the Sabarmati river-bed. In the top 3 m the average SPT is found to be less than 10. In addition to being close to the river-bed it is likely that the top soil might have experienced cyclic softening or partial liquefaction.

Figure 1 shows the grain size distribution curves proposed by Iwasaki (1986) for the liquefaction-susceptible soils and the curves for the Sabarmati-river and Toyoura sands. It is observed that the grain size curves of both types of sands lie within the boundaries of most liquefiable soils. The grain size analysis of the Sabarmati-river sand indicates 91% sand and 9% non-plastic silt. The specific gravity is 2.63, and the maximum and minimum void ratios are 0.65 and 0.35, respectively. The coefficient of uniformity is 4.71 and the coefficient of curvature of the soil is 0.66. The soil is poorly graded sand containing silty fines and has the group symbol SP-SM. The maximum and minimum void ratios of the soil are measured by using the Japanese standard test method (JSA, 2009). In this method, the sand is placed in a cylindrical mould of 60-mm diameter and 40-mm height. The maximum void ratio is determined by pouring the sand through a funnel with 30° angle and 12-mm diameter outlet. The base of the funnel is kept close to the sand surface at all times, as the sand is evenly distributed across the surface. In the case of the minimum void ratio a 20 mm extension piece is added to the mould and the sand is placed in ten layers of 6 mm thickness each. Each layer is tamped manually with 20 blows (such that there are 5 blows on each side) with the amplitude of 50 mm by using a wooden mallet till the required density is achieved. The extension piece is then removed and the sand is levelled by using a straight edge. The results are compared with those of the vibratory table method as per the specifications of IS 2720, Part 14 (BIS, 2006), which are similar to the specifications of ASTM D 4253 (ASTM, 2006a) and ASTM D 4254 (ASTM, 2006b), and there is a very good correlation of the void ratios in both loose and dense states. The CRR of the Sabarmati-river sand is qualitatively compared with that of the Toyoura sand (Tatsuoka et al., 1986). The Toyoura sand has a specific gravity of 2.635, the maximum and minimum void ratios are 0.973 and 0.635, respectively, and D_{50} is 0.21 mm. The grain size analysis data of the Toyoura sand indicates 100% sand. Further, the coefficient of uniformity is 1.533, the coefficient of curvature of the soil is 1.046, and the sand is poorly graded with the group symbol SP. A powerful microscope is used to capture the image of the sand particles. The microscopic view and the morphological analysis (not reported here) indicate that the Sabarmati-river sand particles are subrounded in nature when compared to the Toyoura sand particles.

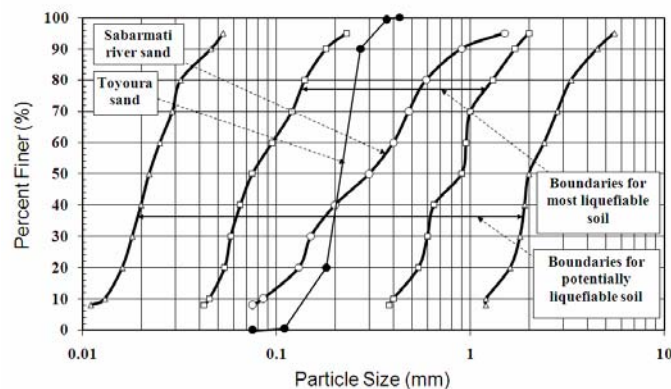


Fig. 1 Grain size distribution curves for liquefaction-susceptible soils, and Sabarmati-river and Toyoura sands (modified after Iwasaki, 1986)

2. Sample Preparation

Triaxial specimens of 50-mm diameter and 100-mm height are prepared by the dry deposition method. This method is adopted as it is not possible for obtaining looser specimens by the other methods (Wood et al., 2008). Wood et al. (2008) have also reported that there are some differences in the undrained response of the silty sand specimens of medium density, but there is no significant variation in

the undrained response of the specimens at higher density due to different depositional methods. Therefore, in order to have a uniform response, the dry deposition method is adopted to prepare the specimens of loose to dense state in the present investigation. In this method the specimen is prepared by placing the spout of the funnel at the bottom of the mould, and then the sand is poured into the funnel. The specimens are prepared in ten layers of equal thickness. In each layer a known mass of sand is poured gently through a sand pouring spout with zero height of fall, so that the sand gets deposited at low energy. To achieve higher densities, constant energy is applied on the sides of the mould for all layers by a wooden mallet. Each layer is tamped manually with 4 blows per layer (such that there is one blow on each side) with the amplitude of 50 mm so as to achieve the desired density. More blows are provided symmetrically to achieve higher densities. The sample is subjected to a small vacuum, and CO₂ gas is passed. Later, de-aired distilled water is circulated through the soil sample. Initially, the samples are subjected to a cell pressure of 100 kPa and a back pressure of 90 kPa, so that the effective confining pressure is 10 kPa, and this condition is maintained till the Skempton's pore pressure coefficient B exceeds 0.96. Then, the specimens are isotropically consolidated at an effective confining pressure of 100 kPa, and the consolidation process is continued till the end of the Casagrande's primary consolidation time. The reduction in the void ratio before and after consolidation is found to be in the range of 0.006 to 0.008. The samples are prepared at the relative densities of 45%, 55%, 62%, 69%, 77% and 85% (the initial relative densities are 43.33%, 53.00%, 59.66%, 65.67%, 75.33% and 83.33%; after consolidation, the samples have the relative densities of 44.67%, 55.33%, 62.06%, 68.96%, 77.18% and 84.75%, which are rounded off to 45%, 55%, 62%, 69%, 77% and 85%, respectively).

3. Stress-Controlled Tests

The testing is performed by using a cyclic triaxial shear test apparatus. The loading system in the apparatus consists of a servo-controlled hydraulic actuator. The amplitude and frequency of the load and waveform are controlled by a function generator. The data is obtained by a computer-controlled data acquisition system. The axial deformation of the soil sample is measured by the LVDTs of ± 10 mm range located outside the cell. The load is measured by a submersible load cell of 5 kN capacity located inside the cell. Further, there are 64 data points per load cycle.

The stress-controlled cyclic triaxial tests are performed under the undrained conditions. A sinusoidal load is applied by a double-acting, equal-area, hydraulic actuator with a total stroke of 100 mm. The actuator carries a state-of-the-art servo valve and the nitrogen-filled accumulators. The tests are carried out at a frequency of 0.1 Hz. This is less than the frequencies generally observed in the earthquake ground motions, but it has been shown that the liquefaction of sand is not frequency dependent (Wong et al., 1975; Wang and Kavazanjian Jr., 1989) and depends instead on the number and amplitude of the cycles of loading, etc. The tests are continued till the sample liquefies, which is characterized by the development of 100% excess pore water pressure ratio or 5% double-amplitude axial strain. After the completion of tests, the specimens are removed carefully from the triaxial cell, such that no particle is lost. Those are then dried and weighed for further calculations.

UNDRAINED CYCLIC BEHAVIOR

1. Experimental Programme

Table 1 shows the details of the program of cyclic tests. A total of 27 cyclic triaxial tests are carried out.

Table 1: Details of Experimental Program

S. No.	Relative Density (%)	Confining Pressure (kPa)	Frequency (Hz)	Cyclic Stress Ratio (CSR)
1	45	100	0.1	0.12, 0.15, 0.18 and 0.184
2	55	100	0.1	0.12, 0.15, 0.17, 0.19 and 0.20
3	62	100	0.1	0.12, 0.14, 0.18, 0.21 and 0.229
4	69	100	0.1	0.14, 0.17, 0.20 and 0.21
5	77	100	0.1	0.18, 0.20, 0.22 and 0.30
6	85	100	0.1	0.19, 0.20, 0.25, 0.30 and 0.33

2. Results and Discussion

2.1 Cyclic Strength

Figure 2(a) shows the deviator stress versus the number of cycles, Figure 2(b) shows the double-amplitude axial strain versus the number of cycles, and Figure 2(c) shows the excess pore water pressure ratio versus the number of cycles, on a sample at $D_r = 55\%$, at 100 kPa confining pressure, and on being subjected to the CSR value of 0.2. The deviator stress is constant on the compression and extension sides. After the third cycle, it is observed that the axial strain increases rapidly and the sample liquefies. The magnitude of double-amplitude strain is very low in the initial stages, and beyond the 0.5% strain level, the double-amplitude strain increases very rapidly. This strain level forms a threshold strain, beyond which there is a faster growth of the strain (or deformation) with cycles. The sample fails at the 5th cycle when the excess pore water pressure becomes equal to the applied confining pressure. At the conditions close to liquefaction, the double-amplitude axial strain is observed to be less than 5%. This may be considered as indicative of the initial liquefaction.

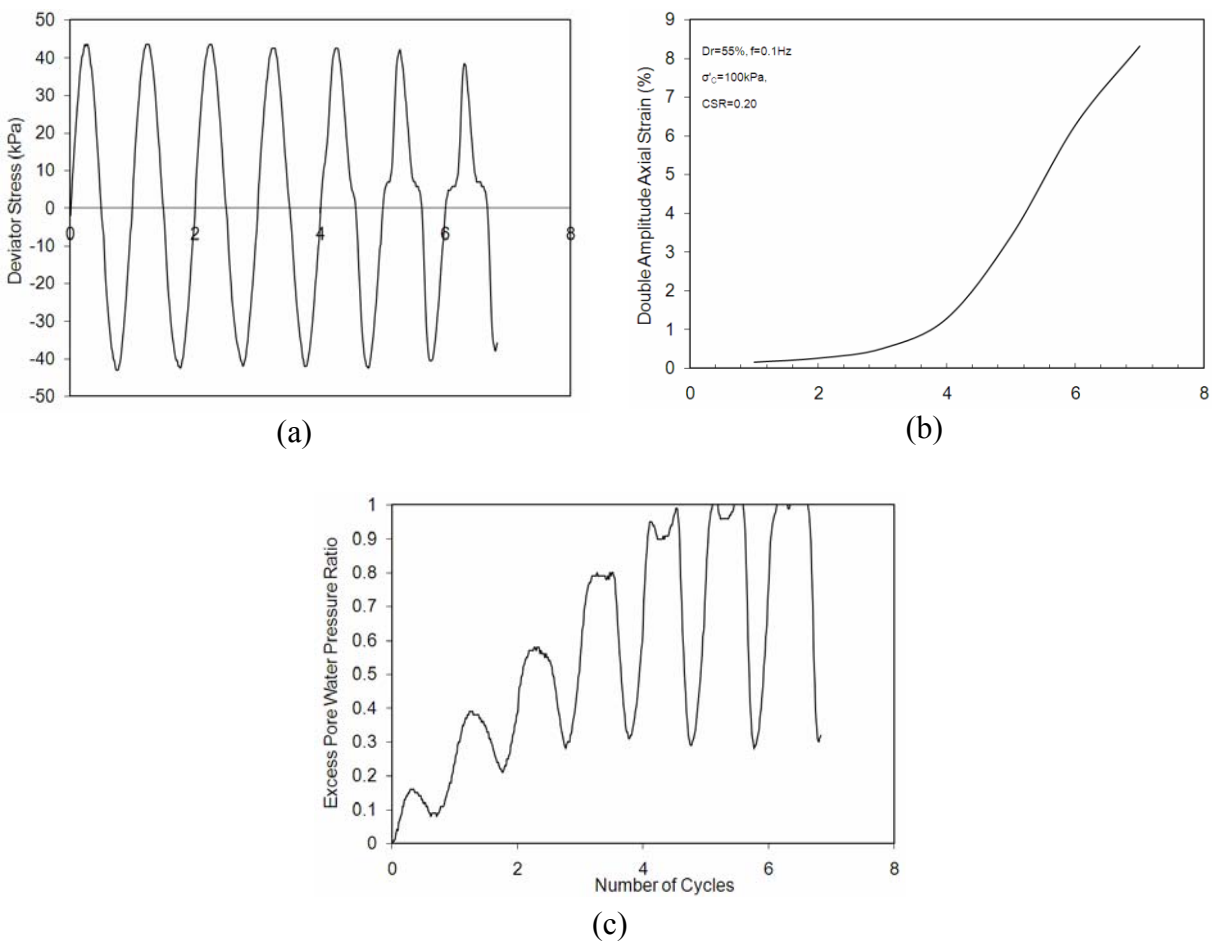


Fig. 2 Cyclic triaxial test results of Sabarmati-river sand sample at loose state having $D_r = 55\%$: a) deviator stress versus number of cycles; (b) double-amplitude axial strain versus number of cycles; (c) excess pore water pressure ratio versus number of cycles

Figure 3(a) shows the deviator stress versus the number of cycles, Figure 3(b) shows the double-amplitude axial strain versus the number of cycles, and Figure 3(c) shows the excess pore water pressure ratio versus the number of cycles, on a sample at $D_r = 85\%$, at 100 kPa confining pressure, and on being subjected to the CSR value of 0.2. The deviator stress is constant on the compression and extension sides. Beyond five cycles, it is observed that the axial strain increases rapidly and the sample liquefies. The magnitude of double-amplitude strain is very low in the initial stages, and beyond the 0.5% strain level, the double-amplitude strain increases rapidly. This strain level forms a threshold strain, beyond which there is a faster growth of the strain (or deformation) with cycles. The sample fails at the 16th cycle, when

the excess pore water pressure becomes equal to the applied confining pressure. At the conditions close to liquefaction, the double-amplitude axial strain is observed to be less than 5% and the sample fails due to the initial liquefaction. The dense sample shows the dilative tendency, as observed by the downward spikes in the pore pressure plot, and this is indicative of the limited potential for large deformations after the initial liquefaction (Baxter et al., 2008).

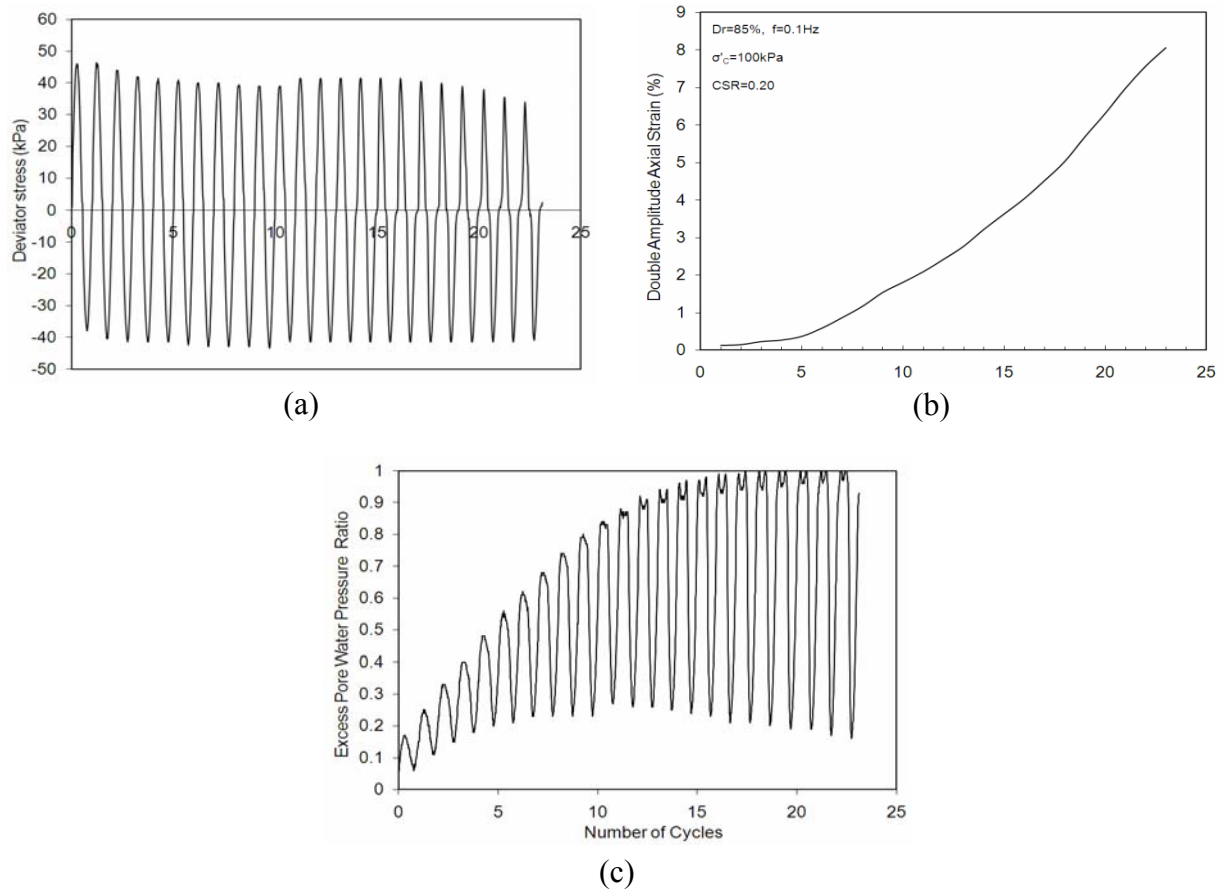


Fig. 3 Cyclic triaxial test results of Sabarmati-river sand sample at dense state having $D_r = 85\%$: a) deviator stress versus number of cycles; (b) double-amplitude axial strain versus number of cycles; (c) excess pore water pressure ratio versus number of cycles

Figure 4 shows the CSR curves for all the relative densities considered in the present investigation. The cyclic strength of sand is specified in terms of the magnitude of CSR required to produce 5% double-amplitude axial strain in the 20 cycles of uniform load application (as described by Ishihara, 1993) and is described as cyclic resistance ratio (CRR). The CRRs are 0.145, 0.16, 0.173, 0.19, 0.225, and 0.296 for the soil samples at the relative densities of 45%, 55%, 62%, 69%, 77%, and 85%, respectively. It is evident from the plot in Figure 4 that the cyclic strength of sand increases as the relative density increases. At low relative densities (i.e., 45% and 55%), the increase in CRR is low, when compared to the increase at higher relative densities (i.e., 77% and 85%).

Figure 5 shows CRR versus relative density curves for the Sabarmati-river and Toyoura sands (Tatsuoka et al., 1986). The Toyoura sand has $e_{max} = 0$, $e_{min} = 0$, and $G = 2$. It is observed that up to a relative density of 70%, CRR tends to increase linearly with an increase in the relative density, but for relative densities greater than 70%, CRR increases at a faster rate. The Sabarmati-river sand shows higher CRRs than the Toyoura sand. Further, the cyclic strength trends for both sands are qualitatively comparable. This clearly brings out the predominant effect of densification on the improvement in cyclic strength.

Figure 6 shows the threshold double-amplitude strain versus the number of cycles curves for various relative densities. The threshold double-amplitude strain is the strain beyond which the deformation increases rapidly. It is observed that when the relative density is higher, this strain is more. In most of the

cases the lower limit of this strain for different stress amplitudes is around 0.5% and above. This implies that when the threshold double-amplitude axial strain is less than 0.5%, the pore pressure build-up will be slow and the sample may not liquefy.

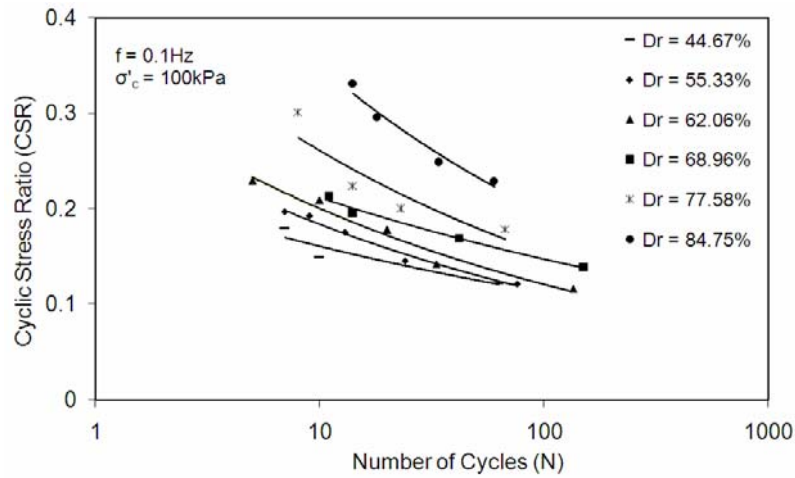


Fig. 4 CSR versus number of cycles curves for various relative densities

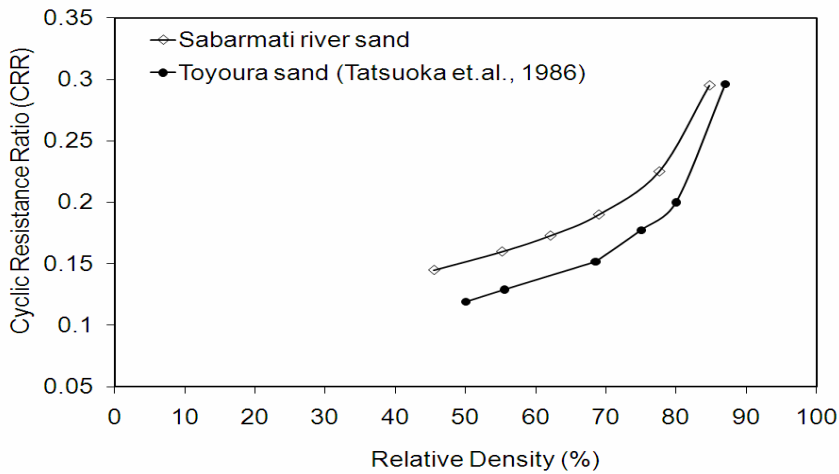


Fig. 5 CRR versus relative density curves for the Sabarmati-river and Toyoura sands

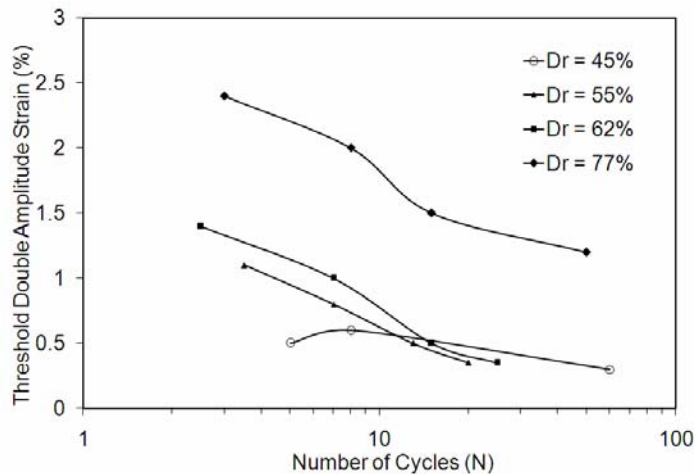


Fig. 6 Threshold double-amplitude strain versus number of cycles curves for various relative densities

Figure 7 shows the comparison of monotonic and cyclic stress paths at the relative density of 62%, corresponding to the void ratio of 0.464, at the 100 kPa confining pressure. The variation of double-amplitude axial strain is also indicated in the same plot. It is observed that when the cyclic stress path is close to the phase transformation line (after the 2nd cycle), the sample deforms rapidly.

Figure 8 shows the deviator stress and excess pore water pressure versus axial strain plots under the monotonic conditions for various relative densities, as obtained from the CU tests. The samples are prepared at the relative densities of 61.67%, 68%, 77% and 84% (after consolidation, the samples have the relative densities of 62.06%, 68.96%, 77.48% and 84.75%, which are rounded off to 62%, 69%, 77% and 85%, respectively). These results indicate that the peak deviator stress increases with an increase in the relative density. All samples with the relative densities greater than 69% show dilation. Therefore, the samples at higher relative densities (i.e., > 70%) show increased negative pore pressures due to the dilation resulting in an increase in the shear strength. For these dilative samples the pore pressure initially increases because of the compressive tendency and then decreases due to the shear. As this continues to decrease further it leads to a negative excess pore water pressure. As a result, the deviator stress increases and attains a peak value. The build-up of negative pore pressures in the samples at high relative densities indicates the possibility of the occurrence of cavitations (Brandon et al., 2006). If there are cavitations, there will be much scatter in the results, when the failure criterion is based on the peak deviator stress. When $\Delta U = 0$ is used as the failure criterion, there will be consistency in the undrained shear strength (Brandon et al., 2006). Therefore, in the present case, the criteria for the peak deviator stress and deviator stress at the critical state (at which the condition of zero pore pressure increment is used) are adopted to obtain the shear strength. Though the peak pore pressure and phase transformation strength criteria are considered for the correlation with CRR, there is much scatter in the results.

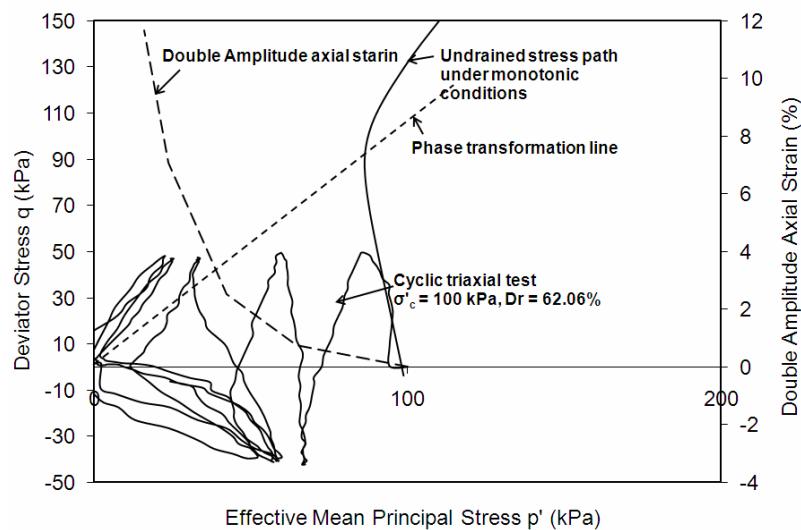


Fig. 7 Comparison of monotonic and cyclic stress paths

Figure 9 shows the CRR versus normalized shear strength plot, as obtained from the monotonic consolidated undrained (CU) tests, where normalized shear strength is the ratio of deviator stress (at the peak or critical state) to twice the effective confining pressure. An excellent correlation is observed between CRR and the normalized shear strength corresponding to the peak or critical state conditions in the CU tests. CRR can be obtained from the monotonic strength by using the following relations:

$$\frac{\sigma_d}{2\sigma'_c} = 0.097 + 0.018 \left(\frac{q_p}{2\sigma'_c} \right) \tag{1}$$

$$\frac{\sigma_d}{2\sigma'_c} = 0.043 + 0.0321 \left(\frac{q_c}{2\sigma'_c} \right) \tag{2}$$

where q_p is the peak deviator stress (in kPa) and q_c is the deviator stress (in kPa) at the critical state, under the monotonic conditions. The results based on the critical state failure criterion are observed to be better than those for the peak deviator stress criterion for the dilative conditions. Equation (1) can be used

for the normally consolidated conditions and Equation (2) is useful for both the normal consolidation and dilative conditions. Further, the undrained strength is equal to the drained strength at the critical state, and Equation (2) provides consistent values of CRR based on the drained and undrained strengths.

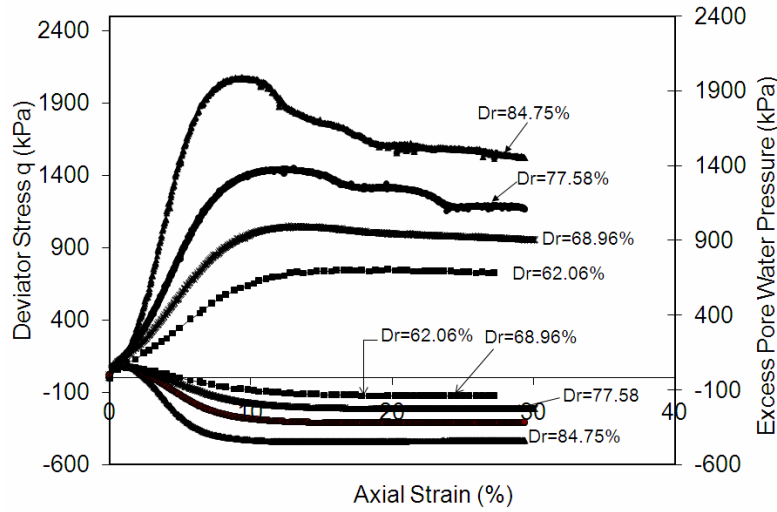


Fig. 8 Deviator stress and excess pore water pressure versus axial strain curves for various relative densities

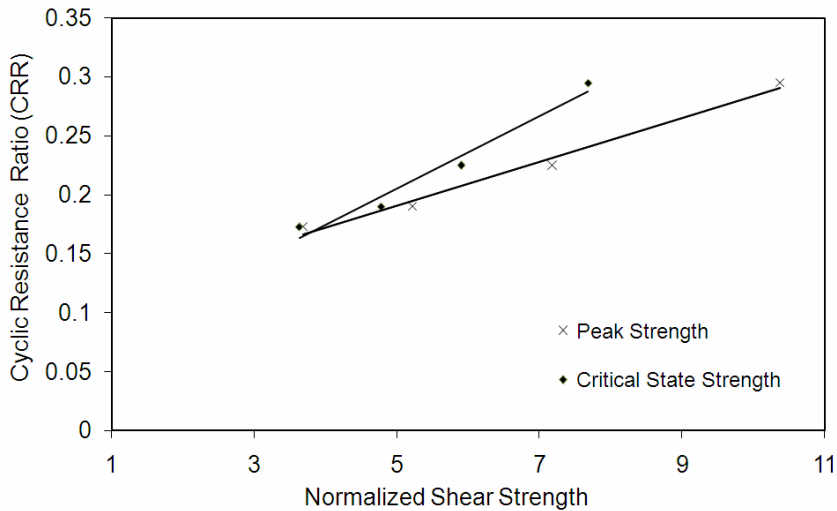


Fig. 9 CRR versus normalized shear strength curves from CU tests

2.2 Pore Pressure Development

Figure 10 shows the residual pore pressure ratio versus cycle ratio (i.e., N/NL) plot for the loose (with the relative density of 45%) and dense (with the relative density of 85%) states with nearly the same CSR values. In addition, the band of pore pressure ratio for all the relative densities and stress ratios in the present investigation is shown along with the data of Lee and Albaisa (1974). The pore pressure ratio is computed based on the residual pore water pressure at zero deviator stress at the end of each loading cycle. It is observed that the pore pressure ratio for the dense sample is more than that for the loose sample at any given cycle ratio till the cycle ratio of 0.55 (corresponding to the compression phase). Beyond this, the loose sample shows a faster build up due to continued compression, whereas the dense sample shows a slow build-up, when compared to the loose sample, due to dilation. The pore pressure band is obtained from 27 tests for a wide range of relative densities from 45% (for the loose state) to 85% (for the dense state). It may be observed that for any given cycle ratio, the pore pressure ratio of the Sabarmati-river sand is more than that reported by Lee and Albaisa (1974).

2.3 Dynamic Properties

Figure 11 shows the shear modulus versus single-amplitude axial strain data points for all the relative densities (from 45% to 85%). The shear modulus is computed here by using the Young’s modulus, where the Young’s modulus is a secant modulus obtained from the experimental data connecting the extreme points of the hysteresis loop. The shear modulus is strain dependent and it decreases with an increase in the axial strain. At low strains (i.e., less than 0.1%), shear moduli appear to increase with an increase in the relative density, but all the moduli are in a narrow band. If the shear modulus is captured at a very low strain, i.e., $\ll 0.01\%$, clear trends can be observed. However, the cyclic triaxial test being a large-strain test facility, the low-strain data cannot be obtained. At large strains, the shear modulus degradation is observed to be independent of the relative density. By about 1% axial strain, the degradation is complete, thus indicating a lower value of the shear modulus. Under the cyclic loading, growth in anisotropy is observed with the reversal of loading. This is reflected in the loss of contacts. This loss of contacts keeps increasing with the reversal of loading, and the effect of density is erased continuously. At large strains, say 1% and above, the system becomes unstable and the sample has the tendency to collapse, as the stiffness decreases due to the growth of anisotropy and the sample is no longer able to withstand the deviator stress. This behaviour has also been captured by the DEM simulations as in Dinesh (2002).

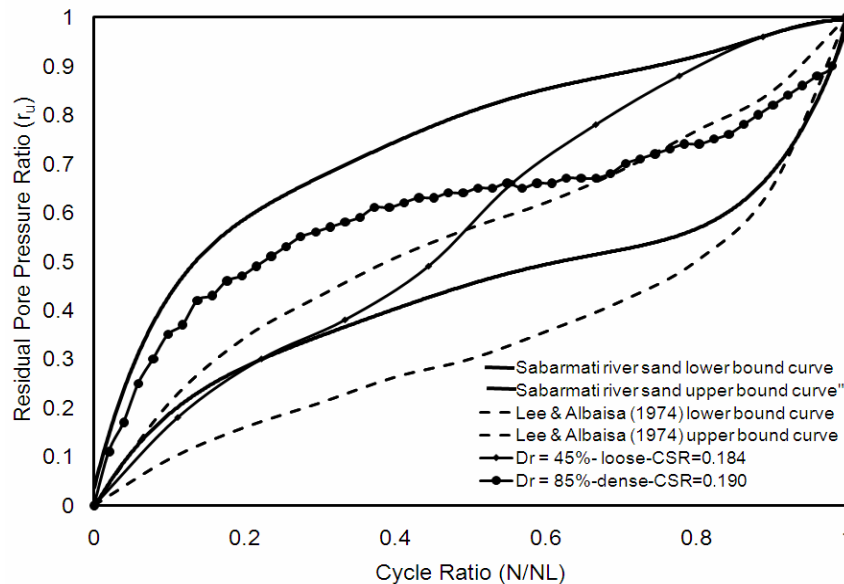


Fig. 10 Residual pore pressure ratio versus cycle ratio curves

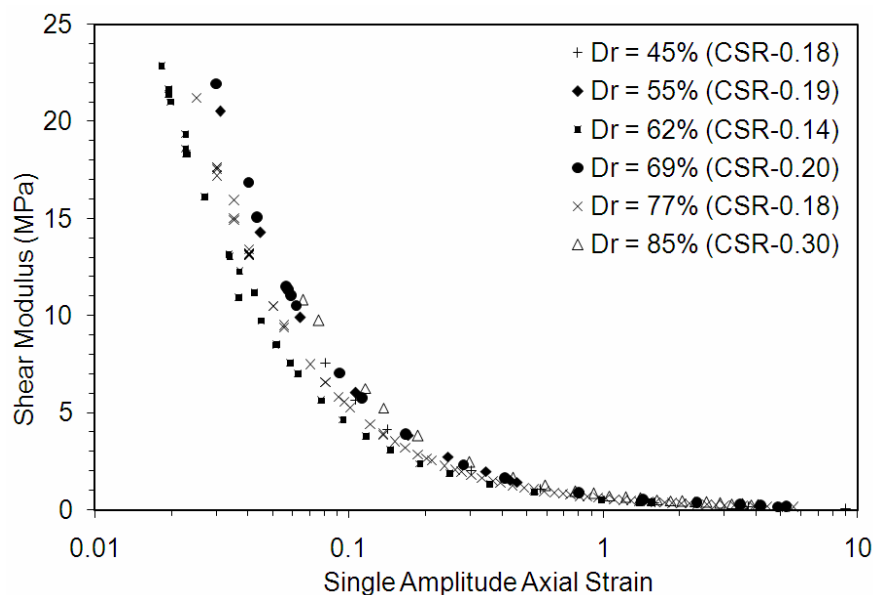


Fig. 11 Shear modulus versus single-amplitude axial strain plot for various relative densities

CONCLUSIONS

A series of undrained cyclic triaxial tests have been performed to evaluate the effects of various factors on the undrained cyclic behavior of the Sabarmati-river sand. Based on the experimental results obtained, the following conclusions have been drawn:

1. The densification of loose sand (with $D_r \leq 70\%$) increases the cyclic strength linearly. The cyclic strength increases suddenly for the dense and very dense sands (with $D_r > 70\%$) due to dilation.
2. There is an excellent correlation between CRR and normalized shear strength (as obtained from the peak and critical state) based on the CU tests. Equations (1) and (2) can be used to predict the cyclic strength from the monotonic tests. Whereas Equation (2) is useful for both the normal consolidation and dilative conditions, Equation (1) can be used for the normal consolidation conditions.
3. The pore pressure build-up in loose sands is uniform, whereas in dense sands the build-up is fast in the initial stages and decreases slightly at the later stages due to dilation.
4. Shear modulus is strain dependent and decreases with an increase in the single-amplitude strain. At low strain levels, shear modulus increases with an increase in the relative density. However, at large strains, the effect of density is erased due to the growth of anisotropy, and all samples, irrespective of their densities, have low shear moduli.

ACKNOWLEDGEMENTS

The authors thank the Ministry of Earth Sciences, Government of India for funding the research project titled “Evaluation of Liquefaction Potential Based on Cone Penetration Resistance and Shear Wave Velocity” (under Grant No. DST/23(534)/SU/2005).

REFERENCES

1. ASTM (2006a). “ASTM D4253-00: Standard Test Methods for Maximum Index Density and Unit Weight of Soils using a Vibratory Table”, ASTM International, West Conshohocken, U.S.A.
2. ASTM (2006b). “ASTM D4254-00: Standard Test Methods for Minimum Index Density and Unit Weight of Soils and Calculation of Relative Density”, ASTM International, West Conshohocken, U.S.A.
3. Baxter, C.D.P., Bradshaw, A.S., Green, R.A. and Wang, J. (2008). “Correlation between Cyclic Resistance and Shear Wave Velocity for Providence Silts”, *Journal of Geotechnical and Geoenvironmental Engineering*, ASCE, Vol. 134, No. 1, pp. 37–46.
4. Bhandari, N. and Sharma, B.K. (2001). “Damage Pattern due to January, 2001 Bhuj Earthquake, India: Importance of Site Amplification and Interference of Shear Waves”, *Proceedings of the International Conference on Seismic Hazard with Particular Reference to Bhuj Earthquake of January 26, 2001*, New Delhi, Abstract Volume, pp. 19–21.
5. BIS (2006). “IS: 2720 (Part 14)-1983—Indian Standard Methods of Test for Soils, Part 14: Determination of Density Index (Relative Density) of Cohesionless Soils (First Revision)”, Bureau of Indian Standards, New Delhi.
6. Brandon, T.L., Rose, A.T. and Duncan, J.M. (2006). “Drained and Undrained Strength Interpretation for Low-Plasticity Silts”, *Journal of Geotechnical and Geoenvironmental Engineering*, ASCE, Vol. 132, No. 2, pp. 250–257.
7. Dinesh, S.V. (2002). “Discrete Element Simulation of Static and Cyclic Behavior of Granular Materials”, Ph.D. Dissertation, Department of Civil Engineering, Indian Institute of Science, Bangalore.
8. Finn, W.D.L. (1981). “Liquefaction Potential: Developments since 1976”, *Proceedings of the First International Conference on Recent Advances in Geotechnical Earthquake Engineering and Soil Dynamics*, St. Louis, U.S.A., Vol. 2, pp. 655–681.
9. Govindaraju, L. (2005). “Liquefaction and Dynamic Properties of Sandy Soils”, Ph.D. Dissertation, Department of Civil Engineering, Indian Institute of Science, Bangalore.
10. Hyodo, M., Hyde, A.F.L. and Aramaki, N. (1998). “Liquefaction of Crushable Soils”, *Geotechnique*, Vol. 48, No. 4, pp. 527–543.

11. Ishihara, K., Tatsuoka, F. and Yasuda, S. (1975). "Undrained Deformation and Liquefaction of Sand under Cyclic Stresses", *Soils and Foundations*, Vol. 15, No. 1, pp. 29–44.
12. Ishihara, K. (1985). "Stability of Natural Deposits during Earthquakes", *Proceedings of the 11th International Conference on Soil Mechanics and Foundation Engineering*, San Francisco, U.S.A., Vol. 1, pp. 321–376.
13. Ishihara, K. (1993). "Liquefaction and Flow Failure during Earthquakes", *Geotechnique*, Vol. 43, No. 3, pp. 351–415.
14. Iwasaki, T. (1986). "Soil Liquefaction Studies in Japan: State-of-the-Art", *Soil Dynamics and Earthquake Engineering*, Vol. 5, No. 1, pp. 2–68.
15. JSA (2009). "JIS A 1224: 2009—Test Method for Minimum and Maximum Densities of Sands (in Japanese)", *Japanese Standards Association*, Tokyo, Japan.
16. Lee, K.L. and Seed, H.B. (1967). "Cyclic Stress Conditions Causing Liquefaction of Sands", *Journal of the Soil Mechanics and Foundation Division, Proceedings of ASCE*, Vol. 93, No. SM1, pp. 47–70.
17. Lee, K.L. and Albaisa, A. (1974). "Earthquake Induced Settlements in Saturated Sands", *Journal of the Geotechnical Engineering Division, Proceedings of ASCE*, Vol. 100, No. GT4, pp. 387–406.
18. Li, X.S., Chan, C.K. and Shen, C.K. (1988). "An Automated Triaxial Testing System" in "Advanced Triaxial Testing of Soil and Rock (edited by R.T. Donaghe, R.C. Chaney and M.L. Silver)", Report STP 977, *American Society for Testing and Materials*, Philadelphia, U.S.A.
19. Polito, C.P. and Martin II, J.R. (2001). "Effects of Nonplastic Fines on the Liquefaction Resistance of Sands", *Journal of Geotechnical and Geoenvironmental Engineering, ASCE*, Vol. 127, No. 5, pp. 408–415.
20. Ravishankar, B.V. (2006). "Cyclic and Monotonic Undrained Behaviour of Sandy Soils", Ph.D. Dissertation, Department of Civil Engineering, Indian Institute of Science, Bangalore.
21. Seed, H.B. (1979). "Soil Liquefaction and Cyclic Mobility Evaluation for Level Ground during Earthquakes", *Journal of the Geotechnical Engineering Division, Proceedings of ASCE*, Vol. 105, No. GT2, pp. 201–255.
22. Tatsuoka, F., Ochi, K., Fujii, S. and Okamoto, M. (1986). "Cyclic Undrained Triaxial and Torsional Shear Strength of Sands for Different Sample Preparation Methods", *Soils and Foundations*, Vol. 26, No. 3, pp. 23–41.
23. Wang, J.N. and Kavazanjian Jr., E. (1989). "Pore Pressure Development during Non-uniform Cyclic Loading", *Soils and Foundations*, Vol. 29, No. 2, pp. 1–14.
24. Wong, R.T., Seed, H.B. and Chan, C.K. (1975). "Cyclic Loading Liquefaction of Gravelly Soils", *Journal of the Geotechnical Engineering Division, Proceedings of ASCE*, Vol. 101, No. GT6, pp. 571–583.
25. Wood, F.M., Yamamuro, J.A. and Lade, P.V. (2008). "Effect of Depositional Method on the Undrained Response of Silty Sand", *Canadian Geotechnical Journal*, Vol. 45, No. 11, pp. 1525–1537.

NEURAL-NETWORK BASED ESTIMATION OF NORMALIZED RESPONSE SPECTRA

C.R. Arjun and Ashok Kumar
Department of Earthquake Engineering
Indian Institute of Technology Roorkee
Roorkee-247667

ABSTRACT

This paper focuses on the application of neural networks as an alternative computational tool for the estimation of normalized response spectra for the horizontal ground motions with magnitudes $M_{JMA} \geq 5$ and hypocentral distances less than 50 km. The feasibility of using the perceptron neural networks in estimating site-specific response spectra and the effects of the geophysical properties of the site is examined. Two neural-network models are proposed for generating normalized response spectra, such that those consider the effects of local site conditions. Model 1 is developed with six inputs (i.e., magnitude, hypocentral distance, primary wave velocity, shear wave velocity, N -values obtained by the standard penetration test (SPT), and density of soil), whereas Model 2 is developed with three inputs (i.e., magnitude, hypocentral distance, and shear wave velocity). As expected, a better performance is obtained from (neural-network) Model 1 in terms of accuracy and efficiency. The results obtained from this study are very encouraging and have a potential to replace the commonly used regression approach.

KEYWORDS: Neural Networks, Response Spectra, Hypocentral Distance, Shear Wave Velocity, Regression Approach

INTRODUCTION

Response spectrum is a fundamental engineering tool in the dynamic analysis and design of structures. The concept of response spectrum, introduced originally by Biot (1941) and later popularized by Housner (1941), describes the maximum response of a series of damped, linear elastic, single-degree-of-freedom oscillators to a particular ground motion as a function of the natural period of vibration or the circular frequency of the oscillator. A response spectrum forms the basis for the structural engineers interested to know the response of structures subjected to a ground motion resulting from an earthquake. For design purposes, seismic codes provide a design spectrum that describes the level of seismic resistance required for design, based on the statistical analysis of the response spectra for an ensemble of ground motions. The design spectrum contains all the information on ground motion amplitudes and frequencies and hence can be directly used to design a structure for earthquake loads (Gupta, 1990). In the past, over 80 studies have been carried out for the estimation of (design) response spectral ordinates (Douglas, 2001, 2002). A majority of the published prediction models for the generation of acceleration response spectra are based on regression analysis.

One of the ways of evaluating site-dependent spectra is by describing the site itself. The most commonly used method to classify sites is according to the shear wave velocity recorded at the recording stations. The literature on the site-dependent spectra is voluminous (e.g., Kuribayashi et al., 1972; Mohraz et al., 1973; Seed et al., 1976; Mohraz, 1976; Trifunac, 1976; Iwasaki et al., 1980; Trifunac, 1990; Lee and Trifunac, 1995; Borchardt, 1994) and hence a review of this literature is not covered in this paper. In this work, an attempt is made to incorporate all the reported site effects at the Kyoshin Net recording stations. Neural networks are used as an alternative tool for generating the response spectral ordinates by using the actual seismic data without any simplifications and assumptions, instead of the commonly used regression approach. To the best of the knowledge of the authors, this is the first time that neural networks are used for estimating normalized response spectra by using the detailed soil properties and site characteristics at the recording stations.

This paper provides a neural-network based approach for estimating the site-dependent response spectra based on earthquake records and site characteristics. The first part of the paper is concerned with the compilation and processing of strong-motion data for the Japanese earthquake records from the

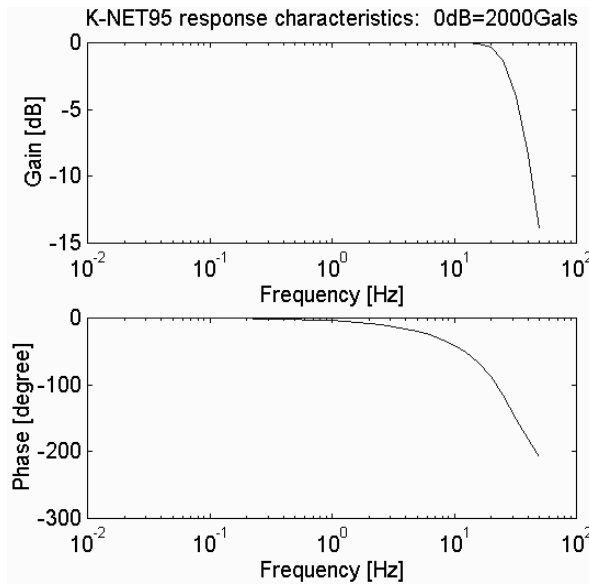


Fig. 2 Response characteristic curves of K-NET95 accelerographs¹

Baseline correction is an important part of the data processing procedure and is essentially required for the correction of errors due to noise. A baseline correction of all uncorrected acceleration time histories is performed by using the least-square line of the time history. Corrections are also applied in frequency domain by filtering the high- and low-frequency components of the accelerograms. All accelerograms are band-pass filtered by removing the frequencies below 0.1 Hz and the frequencies above 30 Hz. A sixth-order Butterworth band-pass function in frequency domain (commonly called as frequency filter) is used for the above filtering operation. For the dynamic analysis of structures, the frequency range of interest is usually below 30 Hz, and hence a frequency limit of 30 Hz is acceptable. The low value of the frequency limit is critical only when the recorded event is in the near-field of a large earthquake. The objective of this study is to use the K-NET database as input to a neural network, and not to study the noise characteristics of the database. Hence, a filter with the band limit of 0.1–30 Hz is applied. As the natural frequency of all accelerographs is very high, there is no need of any instrument response correction.

SITE INFORMATION

The most commonly used parameter to classify the sites is the average shear wave velocity in the top 30 m of the earth, V_{s30} . The National Earthquake Hazards Reduction Program (NEHRP) in USA also uses V_{s30} to define various site categories. K-NET provides the velocity structures beneath the site basically to a depth of 10–20 m by using the downhole measurement method. Apart from the P- and S-wave velocity structures, at each station the N-values of SPT, the bulk density values of soil, and soil profiles are reported. A typical soil data at the recording stations is given in Figure 3. The average values of the shear wave velocity, primary wave velocity, SPT blow count and the density of soil, i.e., \bar{v}_s , \bar{v}_p , \bar{N} , $\bar{\rho}$, respectively, are used as the inputs to a neural network. The averaging is done in accordance with Section 3.5.1 of the NEHRP recommended provisions for seismic regulations for new buildings and other structures (FEMA, 2003):

$$\bar{v}_s, \bar{v}_p, \bar{N}, \bar{\rho} = \frac{\sum_{i=1}^n d_i}{\sum_{i=1}^n \frac{d_i}{v_{si}}, \frac{d_i}{v_{pi}}, \frac{d_i}{N_i}, \frac{d_i}{\rho_i}} \tag{1}$$

where v_{si} denotes the shear-wave velocity of soil, v_{pi} the primary-wave velocity of soil, N_i the SPT blow count, and ρ_i the density of soil, in the layer i ; d_i denotes the depth of the layer i ; and n denotes the number of layers of the similar soil materials, for which data is available.

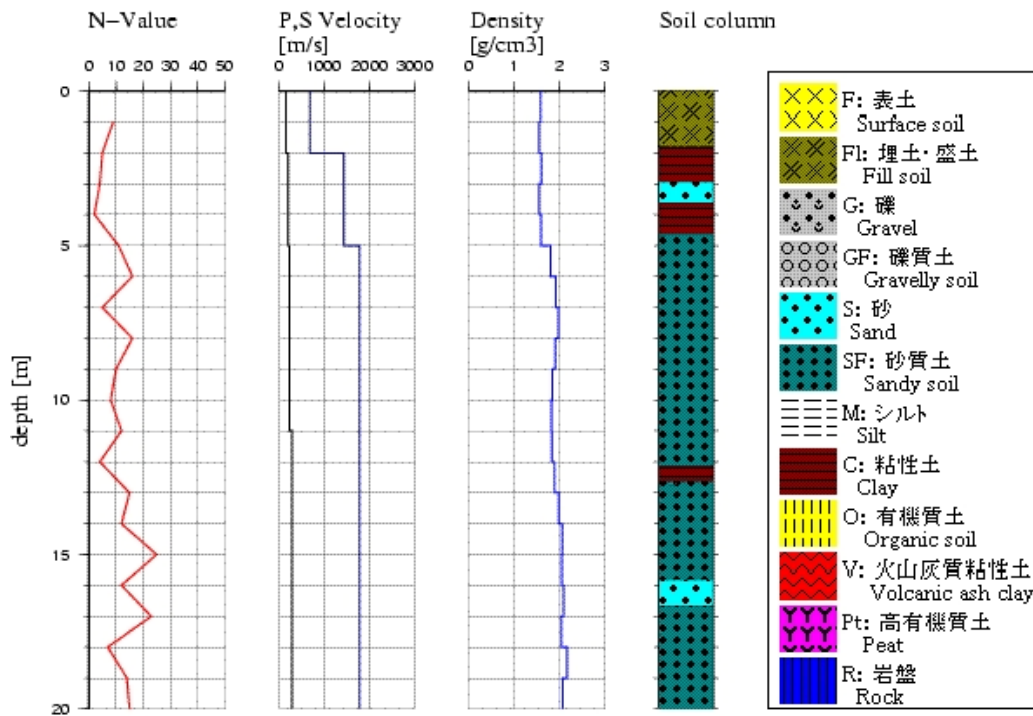


Fig. 3 Site information at FURUDONO site¹

PREDICTIVE MODELS FOR GENERATING RESPONSE SPECTRA USING NEURAL NETWORKS

Artificial neural networks are efficient computing models wherein the solution to a problem is learned from a set of examples. One of the major shortcomings of neural networks is that those are considered as a black box, since there is no satisfactory explanation of their behavior for finding a solution (Benitez et al., 1997). There are many definitions of an artificial neural network (ANN). It is a massively parallel-distributed processor made up of simple processing units, which have a natural tendency of storing experiential knowledge and making it available for use (Haykin, 1994).

The most powerful feature of a neural network involving supervised learning is the input-output mapping. In a supervised learning algorithm the output is known and given to the neural network during the training process so that the neural network can adjust weights in such a way that the actual output moves closer to the desired output. After the training, the neural network is tested by giving only the input values, to see how close its output is to the desired values. Backpropagation is one of the most commonly used algorithms for training the multilayer ANNs. Many researchers have used the multilayer feedforward neural networks in structural dynamics, especially in the field of earthquake strong ground motion problems (e.g., Lee and Han, 2002; Tehranizadeh and Safi, 2004; Ghaboussi and Lin, 1998; Kerh and Chu, 2002; Kerh and Ting, 2005; Kerh et al., 2011). A multilayer neural network consists of an input layer, one or more hidden layers, and an output layer. The relationship between the input and output of a neural network can be linear as well as non-linear. This relationship in any network requires a function, known as the activation function or the transfer function. There are several activation functions, such as step function, linear function, hyperbolic tangent function, and sigmoid function. The transfer functions used in this study are described below.

Hyperbolic Tangent Transfer Function: The hyperbolic tangent transfer function, shown in Figure 4 and used for the hidden units of the multilayer perceptron neural network, has the form $F(x) = \tanh(\alpha x)$, where α is the slope parameter. This function takes the input in form of any value between minus and plus infinity and limits the output to the range $(-1, 1)$.

Sigmoid Transfer Function: The sigmoid transfer function has the form $F(x) = 1/(1 + e^{-\alpha x})$. This transfer function takes the input in form of any value between minus and plus infinity and limits the output to the range $(0, 1)$. This transfer function is used in this study for the output layer and is shown in Figure 5.

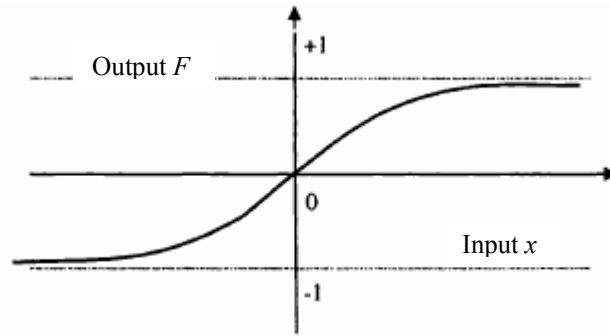


Fig. 4 Hyperbolic tangent transfer function

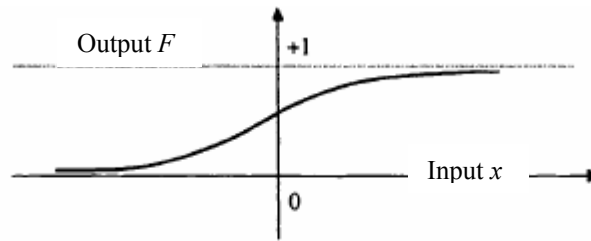


Fig. 5 Sigmoid transfer function

The backpropagation algorithm provides a prescription for changing the weights. The input signal propagates through the neural network in a forward direction, layer by layer. During the forward phase, an input vector is presented to the network, resulting in an output at the output layer. During this phase, the weights are not modified and they are all fixed. In the backpropagation phase the weights are adjusted based on the error between the actual and desired outputs. The hidden layer aids in extracting the higher-order statistics, which tends to be useful when the input layer is large. Also, the use of hidden layer implies that the information needed to compute the output is filtered before passing it on to the next layer. The size of hidden layer is one of the most important considerations, while solving the multilayer feedforward neural networks. Choosing the number of neurons in the hidden layer is an art and is dependent on the complexity of the desired input-output mapping. The following equation is used for the adjustment of connection weights:

$$\Delta w_{ij}(n) = \eta \left(\frac{\partial E}{\partial w_{ij}} \right) + \alpha \Delta w_{ij}(n-1) \quad (2)$$

where $\Delta w_{ij}(n)$ and $\Delta w_{ij}(n-1)$ are the weight increments between the nodes i and j during the n th and $(n-1)$ th epochs (or iterations), respectively, η is the learning rate, and α is the momentum.

The momentum factor and learning rate are used to accelerate the speed of learning without leading to oscillations. The theory of backpropagation algorithm is described in the neural-network related books (e.g., Haykin, 1994; Hagan et al., 1996).

The objective of the training algorithm is to adjust the weights, such that the network performs well, i.e., the quantitative measurement of the network performance decreases. Networks are trained in this study by using the gradient descent with momentum learning scheme, which focuses on using the error between the network output and the desired output. The learning algorithm adapts the weights of the system based on the error until the system produces the desired output. The software NeuroSolutions, Version 5.0 (NeuroDimension, 2003) is used here for the simulation of neural network models. The error criteria family in NeuroSolutions computes the different error measures that can be used to train the network. In this study the criterion used is the L2 norm or the mean squared error (MSE) criterion defined below. In this criterion the squared difference between the system output and the desired signal is simply averaged as

$$\text{MSE} = \frac{1}{2N} \sum_{i=1}^N (x_i - y_i)^2 \quad (3)$$

where x_i and y_i are the actual and predicted values, and N denotes the number of data points in the analysis.

The stopping criterion should be such that it addresses the problem of generalization. This is done by stopping the training at the point of maximum generalization. The training set is usually divided into two sets: the training set and the cross-validation set. The training is stopped when the error in the cross-validation set is smallest. This will be the point of maximum generalization.

A total of 1,850 horizontal components of earthquake records from the Kyoshin Net database of 145 earthquakes, having magnitude M_{JMA} values more than 5.0 and hypocentral distances less than 50 km, are considered in this study. The geometric mean of the two horizontal components at each recording station is considered for the computation of response spectral ordinates. This leads to a set of 925 spectra that will be used for training and testing the neural networks.

1. Implementation Details of Individual Models

For generating a response spectrum by using ANN, neural network models are created in two phases. In the first phase, the magnitude of earthquake, M_{JMA} , hypocentral distance H , average SPT blow count \bar{N} , average primary wave velocity \bar{v}_p , average shear wave velocity \bar{v}_s , and average density of soil, $\bar{\rho}$ are used as the six input variables. In the second phase, a neural network with three nodes on the input layer is created, such that this represents the magnitude of earthquake, M_{JMA} , hypocentral distance H , and the average shear wave velocity \bar{v}_s . In both the phases, the output layer consists of 55 response spectrum ordinates with 5 percent critical damping ratio. Table 1 shows the 55 time periods selected from 0.03 to 10 s for these ordinates. It may be mentioned that in the database considered, the values of M_{JMA} range from 5 to 7.1, H from 0 to 50 km, \bar{N} from 1 to 99, \bar{v}_p from 450 to 3590 m/s, \bar{v}_s from 85 to 1676 m/s and $\bar{\rho}$ from 1125 to 2425 kg/m³.

Table 1: Time Periods Selected for Response Spectrum Ordinates

Period (s)	Ordinate	Period (s)	Ordinate	Period (s)	Ordinate
0.030	RS(1)	0.140	RS(20)	0.900	RS(39)
0.035	RS(2)	0.150	RS(21)	1.000	RS(40)
0.040	RS(3)	0.160	RS(22)	1.200	RS(41)
0.045	RS(4)	0.170	RS(23)	1.400	RS(42)
0.050	RS(5)	0.180	RS(24)	1.600	RS(43)
0.055	RS(6)	0.190	RS(25)	1.800	RS(44)
0.060	RS(7)	0.200	RS(26)	2.000	RS(45)
0.065	RS(8)	0.220	RS(27)	2.500	RS(46)
0.070	RS(9)	0.240	RS(28)	3.000	RS(47)
0.075	RS(10)	0.260	RS(29)	3.500	RS(48)
0.080	RS(11)	0.280	RS(30)	4.000	RS(49)
0.085	RS(12)	0.300	RS(31)	5.000	RS(50)
0.090	RS(13)	0.350	RS(32)	6.000	RS(51)
0.095	RS(14)	0.400	RS(33)	7.000	RS(52)
0.100	RS(15)	0.450	RS(34)	8.000	RS(53)
0.108	RS(16)	0.500	RS(35)	9.000	RS(54)
0.116	RS(17)	0.550	RS(36)	10.000	RS(55)
0.124	RS(18)	0.670	RS(37)		
0.132	RS(19)	0.800	RS(38)		

The total set of 925 spectra is divided into three sets: (1) training set, (2) validation set, and (3) testing set. The training set, consisting of about 80% of the data set, is used to train the network; the validation set, consisting of about 10% of the data set, is used for the purpose of monitoring the training process and to guard against overtraining; and the testing set, consisting of about 10% of the data set and not used in the training process, is used to judge the performance of the trained network. The training is stopped when the cross-validation error begins to increase, i.e., when the cross-validation error becomes minimum.

2. Neural Network Model 1

The ANN model with six nodes on the input layer as described in the previous section is created. A set of 825 spectra is selected randomly from the total set of 925 spectra for training and cross validation, and the remaining spectra are used to test the performance of the trained networks. Four different data sets of 825 spectra are created and randomized. These data sets are trained independently and the data set, which gives the minimum mean-square error (MSE), is considered for testing the network. Parametric studies are carried out in order to evaluate the optimum values of the hidden nodes and learning parameters. The various parameters used for training the network are given in Table 2. Figure 6 shows one hidden layer network model, with 51 hidden neurons, six input neurons and 55 output neurons.

Table 2: Parameters for Neural Network with One Hidden Layer for Six Inputs

Description	Hidden layer	Output layer
Transfer Function	TanhAxon	SigmoidAxon
Learning Rule	Momentum	Momentum
Step Size	1.0	0.1
Momentum	0.7	0.7

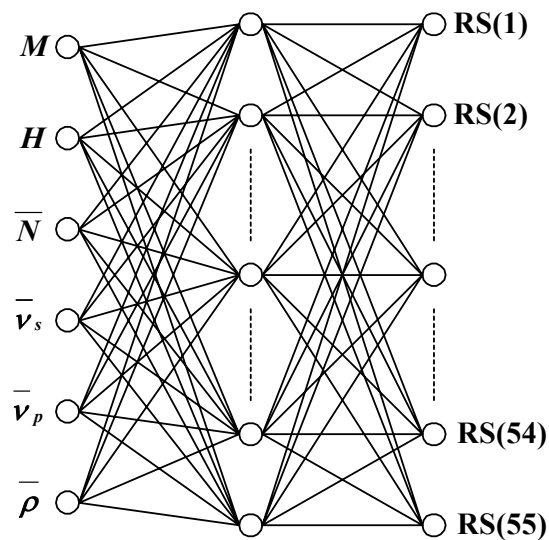


Fig. 6 Neural network architecture with six inputs

The network with 51 hidden nodes in the hidden layer shows the best performance (with minimum MSE). The results obtained after testing the network are compared by plotting the actual and predicted values of the response spectral ordinates. A typical set of results are shown graphically in Figure 7.

The efficiency of results obtained from the tested network is categorized as (a) excellent matching for MSE less than 0.1, (b) very good matching for MSE less than 0.2 and more than 0.1, (c) good matching for MSE less than 0.3 and more than 0.2, and (d) incorrect matching for MSE more than 0.3. The efficiency of results so categorized is tabulated in Table 3. It is observed from this table that the prediction of the trained neural network is quite satisfactory and therefore Model 1 has the potential to fully replace the empirical regression technique. It may be noted that 71% excellent matching is shown by the normalized response spectra predicted by an ANN with six inputs.

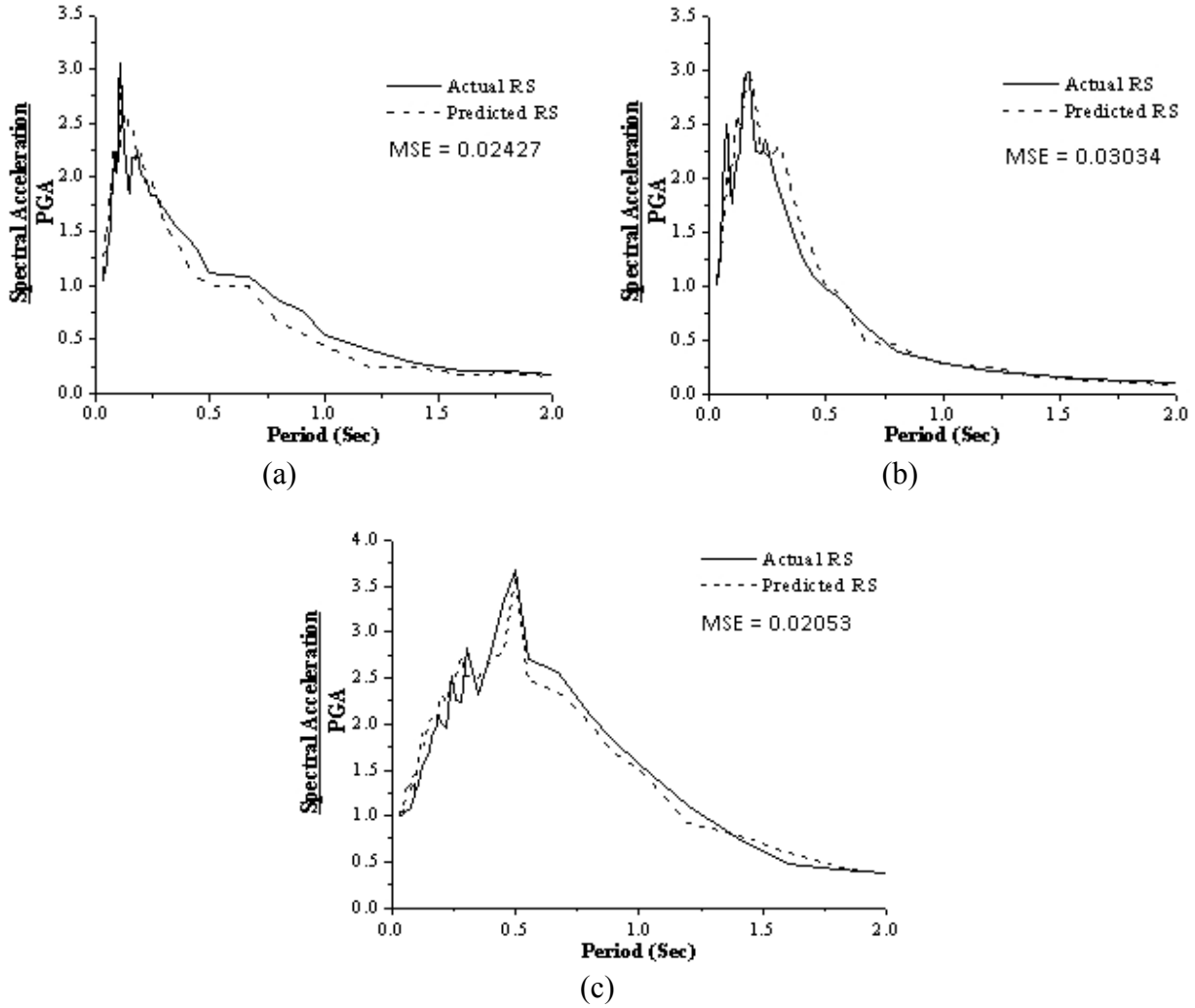


Fig. 7 Typical plots of acceleration response spectra predicted by ANN with six inputs for (a) $M = 5.3$, $H = 30$ km, $\bar{N} = 99$, $\bar{v}_p = 1730$ m/s, $\bar{v}_s = 559.2$ m/s, $\bar{\rho} = 2.1$ g/cm³, (b) $M = 5.0$, $H = 18.3$ km, $\bar{N} = 80$, $\bar{v}_p = 1374$ m/s, $\bar{v}_s = 334$ m/s, $\bar{\rho} = 2.1$ g/cm³ and (c) $M = 5.1$, $H = 31.4$ km, $\bar{N} = 7$, $\bar{v}_p = 930$ m/s, $\bar{v}_s = 124.5$ m/s, $\bar{\rho} = 1.6$ g/cm³

Table 3: Efficiency of Six-Inputs Based Network

S. No.	Efficiency	Percentage
1	Excellent Matching	71
2	Very Good Matching	17
3	Good Matching	8
4	Incorrect Matching	4

3. Neural Network Model 2

Except the K-Net database of Japan, no other country provides detailed soil-condition data at the recording stations. Only few countries provide the values of average shear wave velocity recorded at their recording stations. For the use of trained networks based on the Japanese strong-motion data in other countries, it is essential to train the network with average shear wave velocity representing the site as one of the inputs. Model 2 is developed in a manner similar to that of Model 1, but with only three inputs, i.e., M_{JMA} , H and \bar{v}_s . The network is designed with 3 input nodes, 55 output nodes and 58 hidden nodes (i.e., with the 3–58–55 scheme). The training parameters in Model 2 are similar to those of Model 1. A typical set of results are shown graphically in Figure 8.

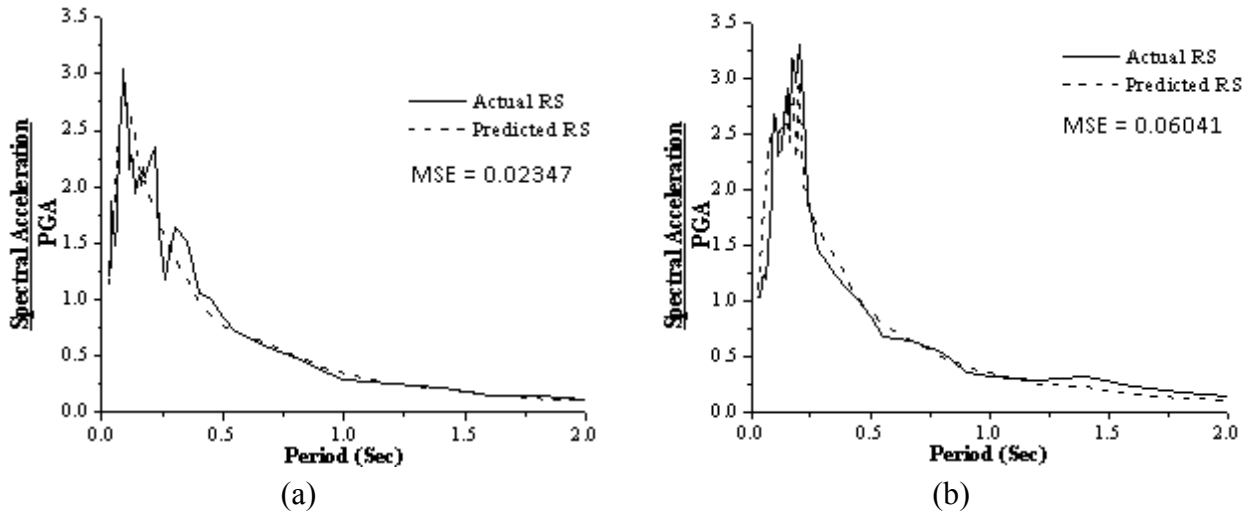


Fig. 8 Typical plots of acceleration response spectra predicted by ANN with three inputs for (a) $M = 5.2, H = 42 \text{ km}, \bar{v}_s = 455.5 \text{ m/s}$ and (b) $M = 5.1, H = 39.6 \text{ km}, \bar{v}_s = 345.8 \text{ m/s}$

The efficiency of results obtained from the tested network is categorized in a similar manner as that for the six inputs and is tabulated in Table 4. It may be observed that with three inputs, 60% of the response spectra predicted show excellent matching. However, the ANN with three inputs is not able to predict sharp variations at the response spectrum peaks.

Table 4: Efficiency of Three-Inputs Based Network

S. No.	Efficiency	Percentage
1	Excellent Matching	60
2	Very Good Matching	20
3	Good Matching	14
4	Incorrect Matching	6

4. Testing of Trained Neural Network Model 2 for Few Significant US Earthquake Motions

As described in the previous section, only few countries provide the values of average shear wave velocity \bar{v}_s recorded at their stations. One such organization is California Strong Motion Instrumentation Program (CSMIP). In this study, processed data from the CSMIP database is considered. It has been found by Katsumata (1996) that the average difference between M_{JMA} and moment magnitude M_w is not significant for the earthquakes in the magnitude range of 5 to 7. The strong-motion records considered from the CSMIP database are (a) Loma Prieta earthquake (with $M_w = 7.0$) of October 17, 1989, recorded at Eureka Canyon road, Corralitos, (b) Big Bear earthquake (with $M_w = 6.4$) of June 28, 1992, recorded at Civic Center grounds, Big Bear lake, (c) Northridge earthquake (with $M_w = 6.7$) of January 17, 1994, recorded at Cedar Hill Nursery A, Tarzana, and (d) Parkfield earthquake (with $M_w = 6.0$) of September 28, 2004, recorded at Gold Hill 3W, Parkfield. The acceleration response spectra predicted by Model 2 for the horizontal motions in these cases are presented in Figure 9. It is observed that the response spectra predicted for these motions (recorded in USA) are quite close to the actual spectra and that MSE is less than 0.1 for the Big Bear, Northridge, and Parkfield earthquake motions and less than 0.2 for the Loma Prieta earthquake motion.

SUMMARY AND CONCLUSIONS

The usefulness of considering the site effects reported by the Kyoshin Net database has been illustrated by implementing neural networks as an alternative predictive tool. Two multilayer perceptron neural network models with back-propagation learning scheme have been generated with variable hidden

layer sizes to predict the 5%-damped normalized response spectra. The prediction abilities of both the neural network models have been tested by using mean-square error as a statistical measure. For Model 1 71% of the predicted normalized response spectra have shown excellent matching (i.e., $MSE < 0.1$), whereas Model 2 has shown excellent matching in 60% cases. Although the neural network models in this study have made acceptable predictions, the accuracy of neural network estimation may need further improvement with the availability of more data sets from different locations and by considering reasonably uniform distribution of records with respect to local site effects while training the network. The models developed here may still serve as a useful guide for evaluating the site-specific response spectra, if detailed information of the local site conditions and potential fault sources are available within a hypocentral distance of 50 km. At the present stage of this study, the effectiveness of perceptron neural network has been demonstrated to predict the 5%-damped normalized response spectra. However, it will be useful to also investigate the applications of the other types of artificial neural networks. Further, in the present study the velocity structure, N -values of SPT and bulk density of soil have been considered over a maximum depth of 20 m and have not been extended to the top 30 m of the earth. However, in future studies it is proposed that these site effects may be extrapolated to at least 30-m depth (Boore, 2004). Also, this study has been limited to the 5%-damped normalized response spectra and therefore it could be extended to include the other values of damping. Another important aspect that could be looked into is the inclusion of fault mechanism as one more additional input to the neural network.

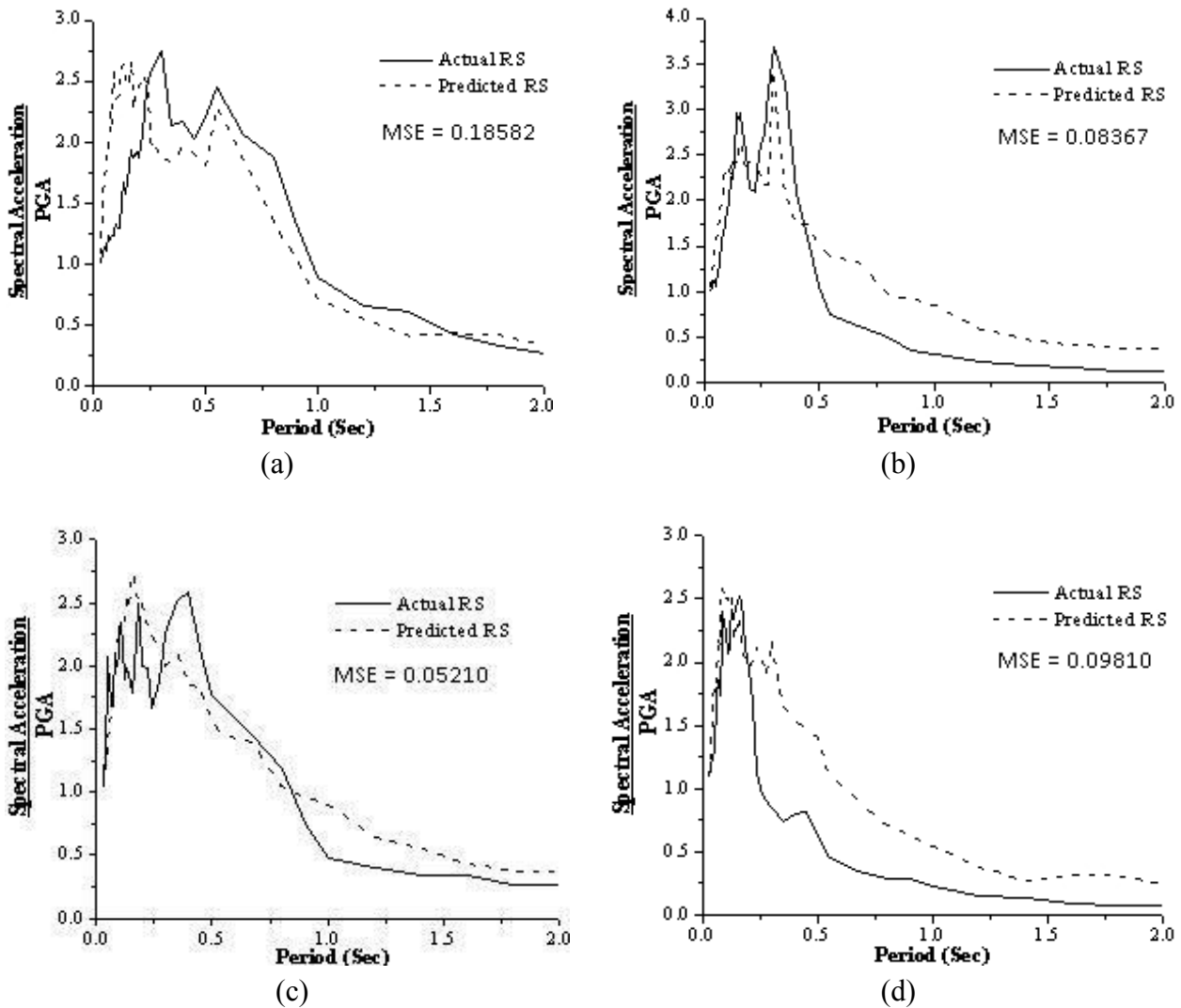


Fig. 9 Acceleration response spectra predicted by Model 2 for (a) Loma Prieta earthquake, (b) Big Bear earthquake, (c) Northridge earthquake and (d) Parkfield earthquake motions

The traditional regression approach models, to predict peak ground acceleration (PGA) and spectral acceleration (SA), have concentrated on finding the standard deviation, which is really a measure of the goodness of fit of the derived relationship with the data used and thus does not provide an insight for the records not used in the regression analysis. However, the proposed neural network models with backpropagation learning have been tested also for some of the records not used for the development of these models. The statistics of the results presented in this work are only for 10% of the data used for testing. Hence, the neural network methodology can be a better alternative and can provide excellent results compared to the conventional regression approach for predicting PGA and SA.

ACKNOWLEDGEMENTS

The authors wish to express their sincere thanks to the Kyoshin Net strong-motion network of Japan for providing us with an excellent earthquake database for conducting this research. In addition, the authors thank the anonymous reviewers for their valuable comments and suggestions to enhance the quality of this article.

REFERENCES

1. Arjun, C.R. (2008). "Application of Artificial Neural Networks for Generating Strong Ground Motion Parameters", M.Tech. Thesis, Department of Earthquake Engineering, Indian Institute of Technology Roorkee, Roorkee.
2. Arjun, C.R. and Kumar, A. (2009). "Artificial Neural Network-Based Estimation of Peak Ground Acceleration", ISET Journal of Earthquake Technology, Vol. 46, No. 1, pp. 19–28.
3. Benitez, J.M., Castro, J.L. and Requena, I. (1997). "Are Artificial Neural Networks Black Boxes?", IEEE Transactions on Neural Networks, Vol. 8, No. 5, pp. 1156–1164.
4. Biot, M.A. (1941). "A Mechanical Analyzer for the Prediction of Earthquake Stresses", Bulletin of the Seismological Society of America, Vol. 31, No. 2, pp. 151–171.
5. Boore, D.M. (2004). "Estimating $\bar{V}_s(30)$ (or NEHRP Site Classes) from Shallow Velocity Models (Depths < 30 m)", Bulletin of the Seismological Society of America, Vol. 94, No. 2, pp. 591–597.
6. Borchardt, R.D. (1994). "Estimates of Site-Dependent Response Spectra for Design (Methodology and Justification)", Earthquake Spectra, Vol. 10, No. 4, pp. 617–653.
7. Douglas, J. (2001). "A Comprehensive Worldwide Summary of Strong-Motion Attenuation Relationships for Peak Ground Acceleration and Spectral Ordinates (1969 to 2000)", ESEE Report 01-1, Civil Engineering Department, Imperial College of Science, Technology and Medicine, London, U.K.
8. Douglas, J. (2002). "Errata of and Additions to ESEE Report No. 01-1: 'A Comprehensive Worldwide Summary of Strong-Motion Attenuation Relationships for Peak Ground Acceleration and Spectral Ordinates (1969 to 2000)'", Department Report, Department of Civil & Environmental Engineering, Imperial College of Science, Technology and Medicine, London, U.K.
9. FEMA (2003). "Recommended Provisions for Seismic Regulations for New Buildings and Other Structures", Report FEMA 450, Federal Emergency Management Agency, Washington, DC, U.S.A.
10. Ghaboussi, J. and Lin, C.-C.J. (1998). "New Method of Generating Spectrum Compatible Accelerograms Using Neural Networks", Earthquake Engineering & Structural Dynamics, Vol. 27, No. 4, pp. 377–396.
11. Gupta, A.K. (1990). "Response Spectrum Method in Seismic Analysis and Design of Structures", Blackwell Scientific Publications, Inc., Boston, U.S.A.
12. Hagan, M.T., Demuth, H.B. and Beale, M. (1996). "Neural Network Design", PWS Publishing Company, Boston, U.S.A.
13. Haykin, S. (1994). "Neural Networks: A Comprehensive Foundation", Prentice-Hall International, Inc., New Jersey, U.S.A.
14. Housner, G.W. (1941) "Calculating the Response of an Oscillator to Arbitrary Ground Motion", Bulletin of the Seismological Society of America, Vol. 31, No. 2, pp. 143–149.

15. Iwasaki, T., Kawashima, K. and Saeki, M. (1980). "Effects of Seismic and Geotechnical Conditions on Maximum Ground Accelerations and Response Spectra", Proceedings of the Seventh World Conference on Earthquake Engineering, Istanbul, Turkey, Vol. II, pp. 183–190.
16. Katsumata, A. (1996). "Comparison of Magnitudes Estimated by the Japan Meteorological Agency with Moment Magnitudes for Intermediate and Deep Earthquakes", Bulletin of the Seismological Society of America, Vol. 86, No. 3, pp. 832–842.
17. Kerh, T. and Chu, D. (2002). "Neural Networks Approach and Microtremor Measurements in Estimating Peak Ground Acceleration due to Strong Motion", Advances in Engineering Software, Vol. 33, No. 11-12, pp. 733–742.
18. Kerh, T. and Ting, S.B. (2005). "Neural Network Estimation of Ground Peak Acceleration at Stations along Taiwan High-Speed Rail System", Engineering Applications of Artificial Intelligence, Vol. 18, No. 7, pp. 857–866.
19. Kerh, T., Huang, C. and Gunaratnam, D. (2011). "Neural Network Approach for Analyzing Seismic Data to Identify Potentially Hazardous Bridges", Mathematical Problems in Engineering, Vol. 2011, Article 464353.
20. Kuribayashi, E., Iwasaki, T., Iida, Y. and Tuji, K. (1972). "Effects of Seismic and Subsoil Conditions on Earthquake Response Spectra", Proceedings of the International Conference on Microzonation, Seattle, Washington, D.C., U.S.A., pp. 499–512.
21. Lee, S.C. and Han, S.W. (2002). "Neural-Network-Based Models for Generating Artificial Earthquakes and Response Spectra", Computers & Structures, Vol. 80, No. 20-21, pp. 1627–1638.
22. Lee, V.W. and Trifunac, M.D. (1995). "Pseudo Relative Velocity Spectra of Strong Earthquake Ground Motion in California", Report CE 95-04, University of Southern California, Los Angeles, U.S.A.
23. Mohraz, B. (1976). "A Study of Earthquake Response Spectra for Different Geological Conditions", Bulletin of the Seismological Society of America, Vol. 66, No. 3, pp. 915–935.
24. Mohraz, B., Hall, W.J. and Newmark, N.M. (1973). "A Study of Vertical and Horizontal Earthquake Spectra", Report WASH-1255 (prepared for U.S. Atomic Energy Commission, Washington, DC, U.S.A.), Nathan M. Newmark Consulting Engineering Services, Urbana, U.S.A.
25. NeuroDimension (2003). "NeuroSolutions: Reference Manual, Version 5.0", NeuroDimension, Inc., Gainesville, U.S.A.
26. Seed, H.B., Ugas, C. and Lysmer, J. (1976). "Site-Dependent Spectra for Earthquake-Resistant Design", Bulletin of Seismological Society of America, Vol. 66, No. 1, pp. 221–243.
27. Tehranizadeh, M. and Safi, M. (2004). "Application of Artificial Intelligence for Construction of Design Spectra", Engineering Structures, Vol. 26, No. 6, pp. 707–720.
28. Trifunac, M.D. (1976). "Preliminary Empirical Model for Scaling Fourier Amplitude Spectra of Strong Ground Acceleration in Terms of Earthquake Magnitude, Source-to-Station Distance and Recording Site Conditions", Bulletin of the Seismological Society of America, Vol. 66, No. 4, pp. 1343–1373.
29. Trifunac, M.D. (1990). "How to Model Amplification of Strong Earthquake Motions by Local Soil and Geologic Site Conditions", Earthquake Engineering & Structural Dynamics, Vol. 19, No. 6, pp. 833–846.

EFFECTIVENESS OF MULTIPLE TSWDs FOR SEISMIC RESPONSE CONTROL OF MASONRY-INFILLED RC FRAMED STRUCTURES

Nishant Kishore Rai*, G.R. Reddy** and V. Venkatraj*

*Directorate of Construction, Services & Estate Management

Department of Atomic Energy, Mumbai-400094

**Bhabha Atomic Research Centre

Department of Atomic Energy, Mumbai-400094

ABSTRACT

An existing masonry-infilled RC framed structure can be retrofitted for improved performance under earthquake loading by the structural response control methodology using tuned sloshing water dampers (TSWDs). The retrofitting may be accomplished by modifying the existing overhead tank, and by installing additional tanks of tuned geometry, for the required response reduction. The required water mass is provided in multiple TSWDs, with their frequencies distributed around the natural frequency of the existing structure. The system as a whole behaves as a multiple-TSWDs retrofitting regime with robustness and reliability. This system takes care of the assessment approximations in the dynamic properties of the existing structure. The proposed retrofitting method aims for reduced displacements during an earthquake. The efficiency of the proposed system may be quantified by its effectiveness ratio. Design charts are developed for reducing the iterative computational efforts. The simplicity of the design and execution of the proposed retrofitting regime is illustrated by the example of an existing four-story structure.

KEYWORDS: Dynamic Magnification Factor (DMF), Mass Ratio, Frequency Ratio, Tuning Ratio, Effectiveness Ratio

INTRODUCTION

Conventional structures have been built to support loads due to gravity only, thus having very little resistance to the lateral forces caused due to earthquakes. The destruction caused in Ahmedabad during the Bhuj 2001 earthquake (EERI, 2001) has exposed the vulnerability of such buildings against earthquakes.

The strengthening and re-qualification of the existing structures against earthquakes is a major area of concern. Most of the existing structures (ES) with ordinary moment-resisting RC frame and masonry-infilled walls have not been designed for earthquake loads. Therefore, these structures are required to be retrofitted. The conventional method of retrofitting an RC framed structure involves the strengthening of its structural components by jacketing and grouting, which may be cumbersome and inconvenient for the occupants of the structure. At the same time the architecture and utility of the building may also be adversely affected.

Another method of retrofitting gaining acceptance lately is of structural response control by incorporating damping devices in the existing structure. As shown in Figure 1, the active, semi-active, hybrid and passive types of damping devices are being used all over the world for structural control (Rai et al., 2009).

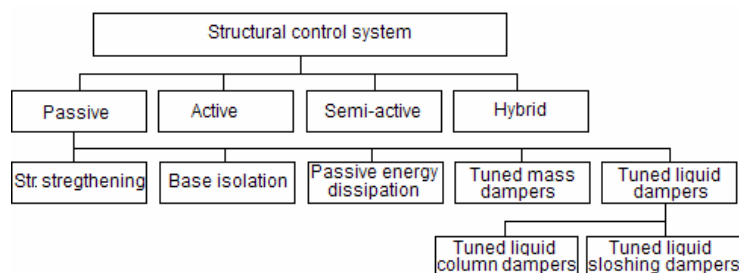


Fig. 1 Structural control systems

The active, semi-active and hybrid types of structural control systems are technology intensive. Further, these systems require an external source of energy for their operation, which may not be available at the required instant of time. In view of these limitations the passive devices are considered more suitable and reliable. Among these, tuned mass dampers (TMDs) and tuned liquid dampers (TLDs) perform by utilizing the damper inertia for energy dissipation. The frequency of the dampers is tuned with the natural frequency of the structure such that the damper mass resonates with the structural motion, thus causing energy dissipation and response reduction under an earthquake excitation.

The theory of TMDs was initially presented for the undamped single-degree-of-freedom (SDOF) systems (Den Hartog, 1956). This concept has been further generalized and optimized for the damped structures (Tsai and Lin, 1993). The 726-ton TMD installed in Taipei 101 is a celebrated example of TMDs, which is designed to reduce the dynamic structural response by more than 30% (Kourakis, 2007). A conventional TMD system requires additional mass and space for its installation. The concept of TMD has been further optimized for practical applicability by isolating a part of the structure to be used as the tuned damping mass. The isolation of the roof of a 13-story building was studied and found feasible for reducing its seismic response (Villaverde, 2000). The roof of an elevated RCC tank has been proposed as a TMD to reduce its response by 20% (Jaiswal, 2004). Two TMD regimes for a 12-story building have been studied by isolating and converting its top two and top four stories respectively as tuned masses along with viscous dampers (Chey et al., 2008). The response control of a 43-story building has been proposed by converting its top floor as a TMD, and a reduction of 20% in its story drifts has been predicted (Makino, 2009). Two case studies have been done for examining the effectiveness of an existing overhead tank (OHT) as a TMD without incorporating any structural changes. It has been analytically found that for 50% or more water in the tank the response of the structure is reduced (Hemalatha and Jaya, 2008).

All the above propositions, for effectiveness, are either applicable to a new structure or require structural modification by the isolation of structural components from the main structure. TLDs are comparatively an easier and more attractive option, wherein the existing water tanks may be utilized as a damping device without any major modifications in the structural systems of the ES (Rai et al., 2010). The evolution of TLDs has been primarily in naval and aerospace engineering. The initial application of TLDs was conceptualized and proposed by W. Froude in 1862, while using two interconnected tanks of tuned frequencies to reduce the rolling motion of a ship (see Figure 2). The actual device was put into application by Sir P. Watts in 1883. Later, a U-shaped tank as roll stabilizer was proposed by Frahm (1911). Further, the response of offshore structures has been reduced by using the mud and crude oil storage tanks as stabilizers (Vandiver and Mitome, 1979). Modi and Welt (1987) were among the first to propose TLD applications for the ground structures. A few parametric studies on TLDs have been presented by Fujino et al. (1988). Thereafter, a number of researchers have studied the behaviour of TLDs. The practical applications of these dampers in the structures like Gold Tower Chiba, Shin Yokohama Prince Hotel, Nagasaki Airport tower and Tokyo Airport tower have shown the response reduction up to 70% at a wind speed of 20 m/s (Tamura et al., 1995). It has been established that for a given mass ratio, a large modal damping in the first mode of vibration may be achieved by tuning for that frequency. A number of tall structures have come up with TLDs for the response control against wind (Rai et al., 2009).

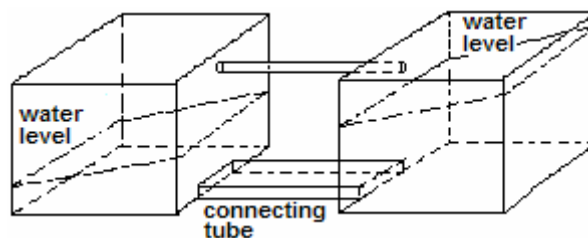


Fig. 2 Interconnected tanks as rolling stabilizer

The theory and analysis of TLDs are dealt on the basis of their analogy with TMDs, where the damper mass is in the form of a liquid (Yalla, 2001). TLDs are classified based on their physical characteristics as tuned liquid column dampers and tuned liquid sloshing dampers. The sloshing dampers with water as the sloshing liquid are termed as tuned sloshing water dampers (TSWDs).

The frequency tuning of the damper mass with the frequency of the structure in ES is vital for the effectiveness of the damping system but is difficult to achieve due to certain assessment approximations in the dynamic properties of the ES. The concept of multiple mass dampers (MMDs), with natural frequencies of the dampers distributed around the assessed natural frequencies of the ES, has been studied for a more robust performance of the dampers. The tuned multiple spatially distributed dampers have shown significant improvement over the performance of a single damper and are more effective in mitigating the motions of the ES under the earthquake excitations. For the same damping mass, the response reduction achieved by multiple dampers (say, five in place of one) is more than that due to a single damper (Kareem and Kline, 1995). A distributed TLD system by filling the hollow floor slabs with water has been found to increase the damping of the structure during the seismic excitations (Lieping et al., 2008). However, this method cannot be applied to the ES. The possibility of converting an OHT as a TSWD has been explored and found to be feasible for retrofitting the ES (Rai et al., 2010).

In this paper seismic retrofitting for the existing medium-height structures is proposed, wherein the existing OHT of the building is modified to the extent that it behaves as a multiple TSWD system. A few additional TSWDs are added at the roof of the building for a further improvement in its performance. The frequencies of the TSWDs are distributed around the estimated frequency of the existing structure to be retrofitted. The effectiveness ratio plots for retrofitting systems with respect to mass ratio, for the realistic ranges of tuning ratio and damping ratio, are developed. These charts reduce the computational demand and make the design methodology very simple. The proposed method is illustrated with the example of an existing structure.

STRUCTURAL RESPONSE CONTROL: GENERAL CONCEPT

The response of an SDOF structure under seismic excitations is governed by its in-built structural properties, mass m_s , stiffness k_s , and damping c_s . The derived dynamic properties of the structure are its natural frequency ω_s and damping ratio ξ_s , expressed as

$$\omega_s = \sqrt{k_s/m_s} \tag{1}$$

and

$$\xi_s = c_s/2m_s\omega_s \tag{2}$$

The influences of frequency and damping ratio on the response are incorporated in the design procedures through response curves (e.g., see Figure 3). A typical 5% damping ratio is implicit in the code-specified earthquake forces and design spectra (Chopra, 1995). A response correction factor is therefore suggested by Nawrotzki (2005) for a damping ratio other than 5% (see Figure 4). It is evident from Figures 3 and 4 that the response of a structure may be reduced by increasing its damping. With an increase in deformation, the inherent damping ratio also increases, but the stiffness of structure gets reduced (Chopra, 1995). This may be detrimental to the structure and should be avoided during a seismic event. The damping ratio of the ES can be increased without a loss of stiffness by incorporating a supplemental energy dissipater in the structural systems.

The time-dependent energy relationship during a seismic event may be expressed as

$$E(t) = E_k(t) + E_s(t) + E_h(t) + E_d(t) \tag{3}$$

where $E(t)$ represents the total energy input due to the earthquake, $E_k(t)$ represents the absolute kinetic energy, $E_s(t)$ represents the (recoverable) elastic strain energy, $E_h(t)$ represents the irrecoverable energy dissipated through inelastic, viscous and hysteretic actions, and $E_d(t)$ represents the energy dissipated by the supplemental damping system, at the time t . If D_m represents the deformation of the existing structure without any retrofitting measure, the deformation D_p after retrofitting (i.e., the installation of TSWDs) may be restricted to the maximum permissible deformation, i.e., $D_p < D_m$, for designing the TSWDs.

In conventional structures (see Figure 5(a)) $E_d(t)$ is not present. The input energy from the earthquake is, therefore, transformed into the kinetic and strain energies and is dissipated through the

inherent energy dissipation capacity of the structure by the hysteretic actions represented by the damping ratio ξ_s of the structure. By attaching an energy dissipating device, such as TSWD, to the structure (see Figure 5(b)), a portion of the input seismic energy $E_d(t)$ is absorbed by this device. This results in a reduced response (i.e., D_p) of the structure. This phenomenon may be quantified through an increase in the effective damping ratio of the structure as a whole.

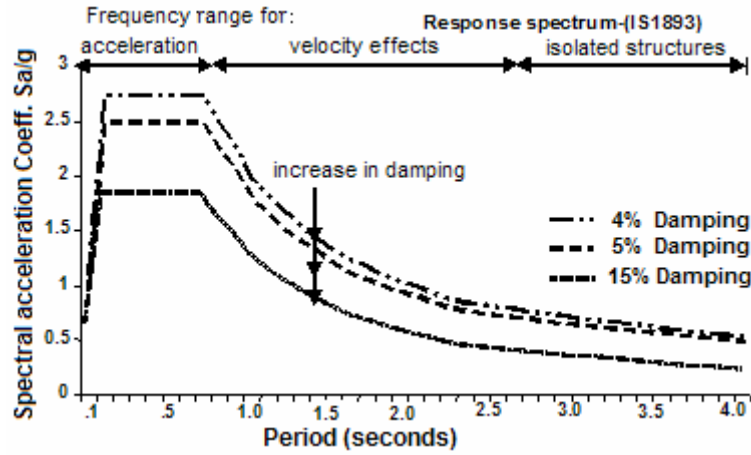


Fig. 3 Acceleration response spectrum for ground motion

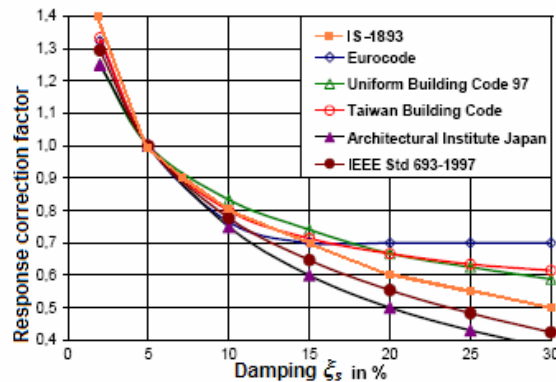


Fig. 4 Effect of damping ratio on structural response

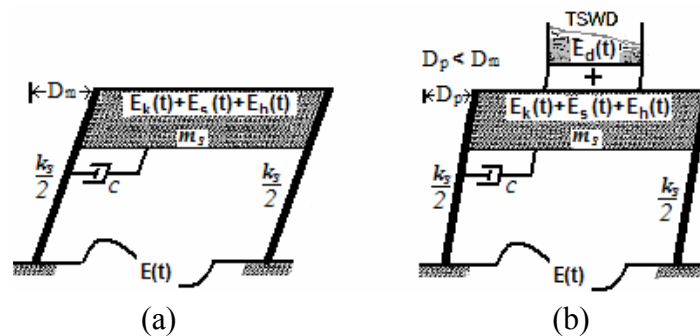


Fig. 5 Seismic energy equations of (a) conventional structure and (b) structure with damping device

PROPERTIES OF TUNED SLOSHING WATER DAMPERS

A tuned sloshing damper with water as the sloshing liquid (i.e., TSWD) is the simplest form of the passive devices belonging to the family of tuned liquid dampers. A TSWD consists of a rigid vessel holding a given mass of water and placed at the top of the building (see Figure 6(a)). The water in the

tank is tuned with the natural frequency of the supporting structure. The sloshing mass of the water thus resonates with the motion of the supporting structure. The energy dissipation here is caused by the sloshing of water contained in the vessel. A part of the seismic energy imparted to the structure is dissipated by the sloshing motion of the water, thereby modifying the resultant structural response within the acceptable limits. TSWDs have been viewed and explained as a variant of tuned mass dampers (TMDs), wherein water is the damping mass. A simplified model of liquid sloshing in tanks has been described by Reddy et al. (2008), based on the equivalent mechanical analogy with lumped masses, springs (for stiffness) and dashpot (for viscosity) (see Figure 6(b)).

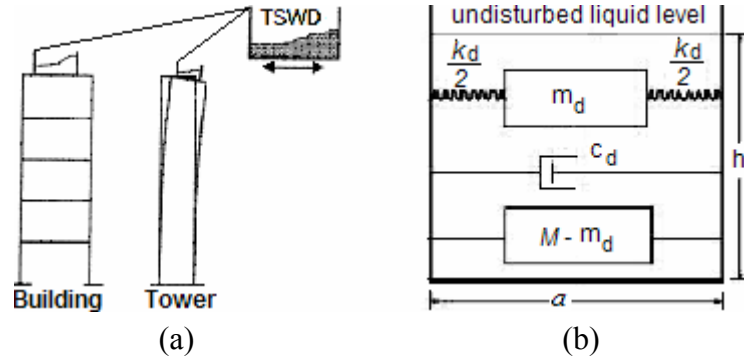


Fig. 6 (a) TSWD on structure; (b) Mechanical analogy for TSWD

The frequency of the sloshing water in a TSWD is given on the basis of linear wave theory as (Abramson, 1966)

$$\omega_n^2 = \frac{g(2n-1)\pi \tanh(2n-1)\pi r}{a} \quad (4)$$

This equation is valid for small excitation amplitudes. At larger excitation amplitudes, the behaviour of the sloshing water becomes nonlinear and the nonlinear frequency ω_d is determined by the following empirical relations (Yu et al., 1999):

$$\omega_d = \omega_n \left\{ 1.037 \left(A_e/a \right)^{0.0035} \right\} \text{ for } A_e < 3\% \text{ of the tank dimension } a \quad (5a)$$

$$\omega_d = \omega_n \left\{ 1.59 \left(A_e/a \right)^{0.125} \right\} \text{ for } A_e > 3\% \text{ of the tank dimension } a \quad (5b)$$

The mass m_d of the sloshing water is given by the potential flow theory as (Graham and Rodriguez, 1952)

$$m_d = M \frac{8 \tanh \left\{ (2n-1)\pi r \right\}}{r\pi^3 (2n-1)^3} \quad (6)$$

where ω_n is the linear sloshing frequency of the water in rad/s, ω_d is the nonlinear sloshing frequency of the water (i.e., the frequency of the TSWD) in rad/s, n is the sloshing mode number (taken as 1 for the natural frequency), M is the total mass of the water in the tank, m_d is the mass of water acting in the considered mode (i.e., the sloshing mass), g is the gravitational acceleration, h is the depth of water in the tank, a is the tank dimension in the direction of vibration, $r = h/a$, A_e is the vibration amplitude of the TSWD, which is equal to the structural displacement at the location of the TSWD, and ξ_d is the damping ratio of the TSWD.

The damping due to the viscosity of water in linear sloshing alone is of the order of 0.5%. However, from experimental experience it has been substantiated that the energy dissipated in a TSWD, due to non-linear sloshing and wave breaking, is much more. The damping ratio ξ_d of a TSWD is a function of the amplitude of excitation and the tank dimension A_e/a . The empirical relationships for TSWD damping ratio have been proposed as

$$\xi_d = 1.78(A_e/a)^{0.68} \quad (7a)$$

and

$$\xi_d = 0.5(A_e/a)^{0.35} \quad (7b)$$

by Yalla (2001) and Yu et al. (1999), respectively. The values of ξ_d as obtained from both the equations are comparable at small vibration amplitudes. The variation of ξ_d with A_e/a is plotted in Figure 7 for Equations (7a) and (7b). For brevity a mean of both is also plotted in the figure and is considered in the present study.

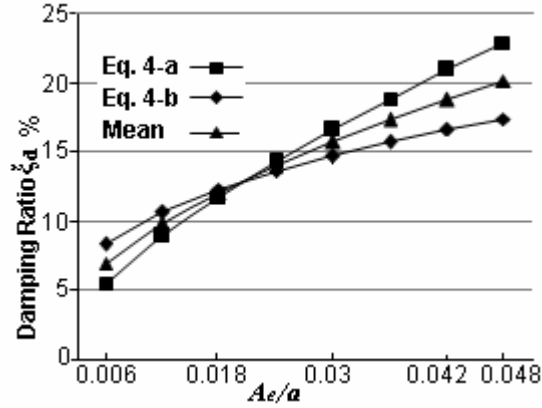


Fig. 7 Damping ratio of TSWD with respect to amplitude of excitation

RESPONSE CONTROL WITH TSWD FOR EXISTING STRUCTURES

The RC structures are assumed to possess a damping ratio of 5%. The analytical approach for a damped structure coupled with a damped damper (i.e., TSWD) is adopted for the retrofitting of the ES. A reasonably planned structure exhibits a substantial mass participation in its first mode of vibration. The ES may be assumed as the SDOF system corresponding to the first-mode frequency ω_s , participating mass m_s and damping ratio ξ_d . The dynamic magnification factor (DMF), denoted by H , for the structural response D_m of the damped SDOF under a harmonic excitation is given by

$$H = \frac{1}{2\xi_s(1-\xi_s^2)^{0.5}} \quad (8)$$

For all realistic purposes,

$$\xi_s = 1/2H \quad (9)$$

is considered to be a reasonable approximation for the ES. By attaching a TSWD with the ES, the coupled system becomes a 2-DOF system, as shown schematically in Figure 8. The TSWD has the mass m_d , stiffness k_d , viscous damping c_d , frequency ω_d and damping ratio ξ_d .

The DMF H_e of the retrofitted structure (i.e., a 2-DOF system) for the reduced structural response D_p is given as

$$H_e = \frac{1}{\sqrt{RE^2 + IM^2}} \quad (10a)$$

where

$$RE = 1 - \beta^2 - \mu\beta^2 \frac{f^2 \{f^2 - \beta^2 + (2\xi_d\beta)^2\}}{(f^2 - \beta^2)^2 + (2f\xi_d\beta)^2} \quad (10b)$$

$$IM = 2\xi_s\beta + \frac{2\mu\beta^5}{(f^2 - \beta^2)^2 + (2f\xi_d\beta)^2} \tag{10c}$$

$\beta = \omega_e/\omega_s$ is the frequency ratio, $f = \omega_d/\omega_s$ is the tuning ratio, and $\mu = m_d/m_s$ is the mass ratio. The equivalent damping ratio ξ_e of the coupled structure may be obtained as

$$\xi_e = \frac{1}{2H_e} \tag{11}$$

where H_e and ξ_e depend on f , μ , β , ξ_s and ξ_d . The effects of these parameters for a tuned coupling of damper and structure (i.e., $f = 1$ or $\omega_s = \omega_d$) with respect to frequency ratio are illustrated in Figure 9.

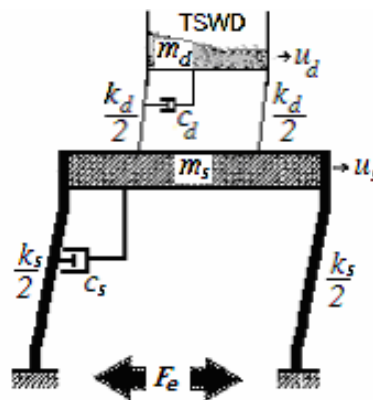


Fig. 8 Structure retrofitted with TSWD

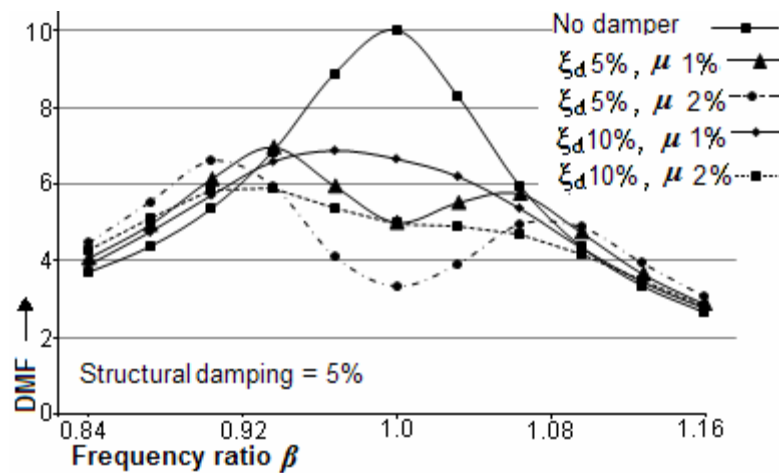


Fig. 9 Dynamic magnification factor for SDOF system with damper

The ES-TSWD coupling is considered detuned if $\omega_s \neq \omega_d$. The dynamic properties of ES are generally beyond the scope of any alterations. The remaining controllable parameters in the ES-TSWD coupling therefore are ω_d , m_d and ξ_d . The performance of the retrofitting system is governed by these parameters. The dampers of small damping ratios are more sensitive to the tuning with the host structures (i.e., ES), whereas the dampers of high damping ratios are comparatively robust with respect to the frequency tuning. An increase in the mass ratio reduces DMF, thus resulting in a higher structural response control. The design of the TSWD-retrofitted ES coupling is governed by Equations (10a)–(10c). The mutual tuning of the ES with TSWD is vital, but difficult to be achieved due to the approximations involved in the assessment of the dynamic properties of ES. This problem may be addressed by the concept of multiple TSWDs, as explained in the following sections.

MULTIPLE TSWDs FOR EXISTING STRUCTURES

The stiffness of the ES is derived from the cross-sectional properties of structural elements and elastic properties of the construction material, which may not be uniform as assumed in the design calculations. The mass of the structure may also vary due to the constructional and utility variations of the ES. These factors lead to a variation in the first-mode frequency assessment of the structure. Similarly, the damping ratio of a building cannot be assessed accurately as it depends on a number of factors. The damping ratio of the ES also varies with the nature of loading and deformation of ES.

The above-mentioned approximations are carried over to the estimated response of the structure. The problem is compounded by the fact that the natural frequency and damping ratio of the TSWD are dependent on the amplitude of vibration, which is same as the displacement of the ES at the location of the TSWD. These approximations may lead to an erroneous design of the TSWD and less effective response-control performance of the retrofitting system. This difficulty may be addressed by extending the concept of multiple mass dampers (MMDs) to TSWD (see Figure 10).

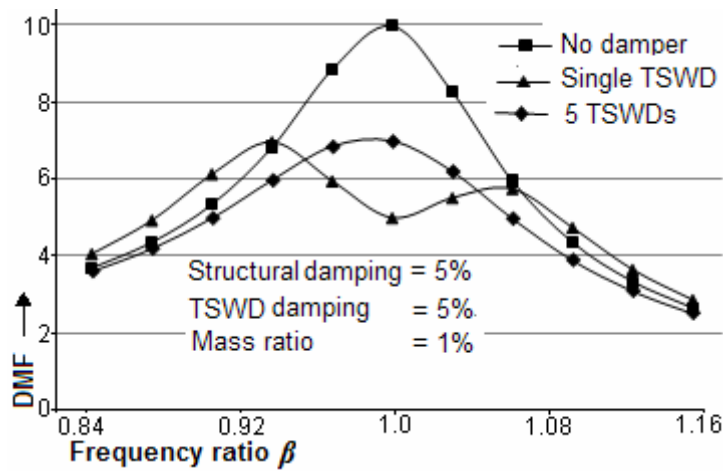


Fig. 10 Dynamic magnification factors for single and multiple TSWDs

The required sloshing mass for the desired results is large enough and multiple TSWDs are provided to meet this requirement. The natural frequencies of these TSWDs are varied and set around the assessed first-mode frequency of the ES. This can be achieved by slightly varying the length a of the TSWD (see Equations (4), (5a) and (5b)). The method of multiple TSWDs ensures that some part of the sloshing mass is always tuned with the ES and a major portion of the sloshing mass is only slightly detuned. Thus, a robust structural control performance is achieved at the same mass ratio. This concept is illustrated in Figure 10, with multiple TSWDs having 5 discrete frequencies as $\omega_d = 0.88\omega_s$, $0.94\omega_s$, $1.0\omega_s$, $1.06\omega_s$ and $1.12\omega_s$. The mass ratio assigned to each TSWD is 0.2μ . It can be observed that the multiple-TSWD system is more effective for a wider range of frequencies and tuning ratios.

EFFECTIVENESS RATIO CHARTS

The efficiency of the TSWD retrofitting system may be expressed by a non-dimensional parameter, effectiveness ratio E . This parameter may be expressed as a percentage reduction in the structural displacement (from D_m to D_p) due to the application of the retrofitting measure:

$$E = \left\{ 1 - \left(D_p / D_m \right) \right\} \times 100 \quad (12a)$$

or

$$E = \left[1 - \left\{ DMF_r / DMF_o \right\} \right] \times 100 \quad (12b)$$

where DMF_o denotes the dynamic magnification factor of the unretrofitted structure and DMF_r denotes the dynamic magnification factor of the retrofitted structure. The effectiveness ratio of a TSWD

retrofitting system depends on ξ_s , ξ_d , f and μ . The performance charts for the condition of maximum DMF, i.e., $\beta = 1$, and a pre-determined detuning range are developed from Equations (10a)–(10c), (12a) and (12b). Detuning here is defined as the percentage difference between the frequencies ω_s and ω_d of the ES and TSWD, respectively.

Three performance charts are plotted for the TSWD damping ratios of 8%, 12% and 20% in Figures 11(a)–11(c) for the structural damping ratios of 2%, 5% and 7%, respectively. The range considered for detuning is 16% (i.e., f ranges from 0.84 to 1.16). The solid lines in the charts are for the perfectly tuned conditions and the dotted lines are for the detuning of 16%. The intermediate values may be interpolated from these curves. These performance charts take care of the approximations involved in the assessment of the dynamic properties of the ES and facilitate a quick estimate of the required μ for the desired effectiveness E of the retrofitted structure. The retrofitting procedure with an application of the effectiveness performance charts is explained below with the example of an existing structure.

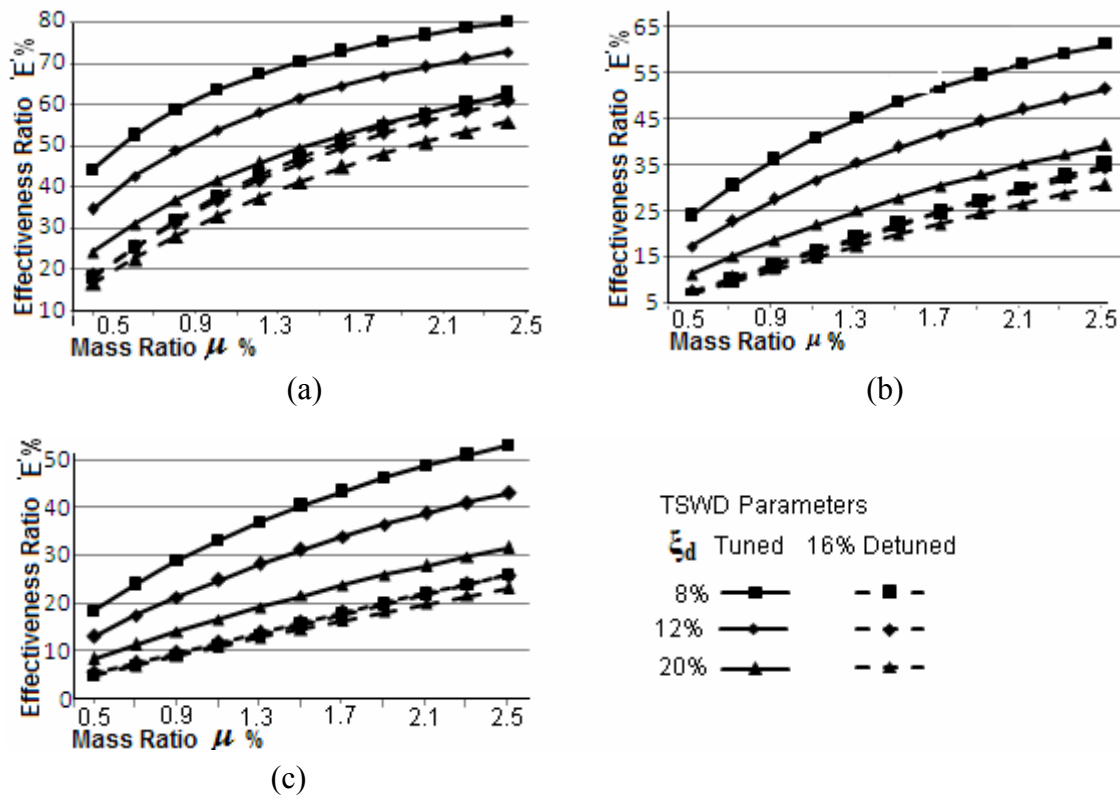


Fig. 11 Performance charts of TSWD system with respect to μ and ξ_d for (a) 2% structural damping ratio, (b) 5% structural damping ratio and (c) 7% structural damping ratio

RETROFITTING OF EXISTING STRUCTURE

1. Details of Structure

An existing four-story residential structure is considered as an example for the study of retrofitting with TSWDs. It is situated in Mumbai, and houses 8 flats with a centrally located staircase, over which an overhead tank (OHT) is placed. The supporting frame of the OHT is a part of the main RC structural framework. The structure is an adequately designed and constructed building, with due consideration of the prevalent code provisions as per IS 456 (BIS, 2000).

The typical floor plan and structural skeleton are shown in Figures 12 and 13, respectively. All the columns here are of the 250×350 mm cross-section, except for the column No. B3, which is of the 250×500 mm cross-section. A typical beam cross-section is 230×400 mm along the X-axis and 230×450 mm along the Z-axis. The positioning of the beams has been done in compatibility with the architectural requirements. The masonry is of burnt-clay bricks with 1:4 cement-sand mortar. The

external walls are 230-mm thick and the internal partition walls are 115-mm thick. Salient design features considered in the analysis are tabulated in Table 1. The example structure may be considered as a representative sample of the well-designed and constructed residential building stock.

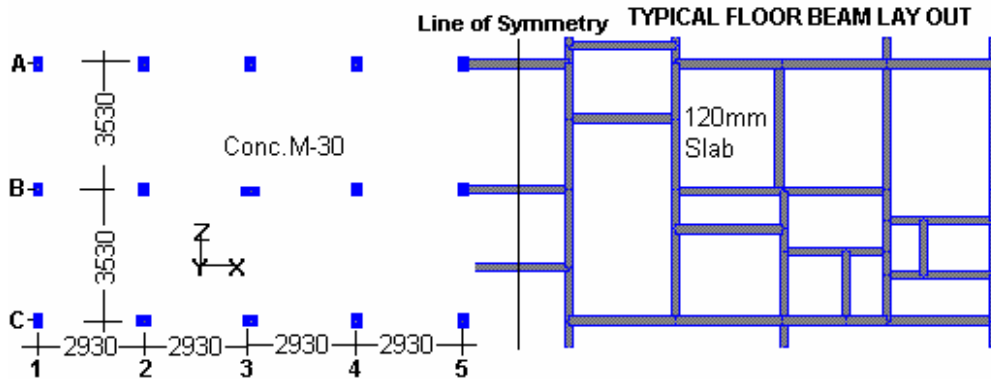


Fig. 12 Structural floor plan of existing structure

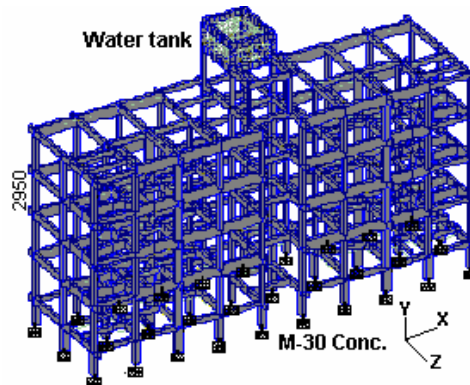


Fig. 13 RC frame of existing structure

Table 1: Salient Features of Existing Structure

S. No.	Feature	Description
1	Total Weight of Structure	11,64,000 kg with water tank full
2	Mass Participating in First Mode, m_s	76% (or 8,85,000 kg)
3	Structural Damping ξ_s	5% (as considered in design)
4	Seismic Zone	III as per IS 1893, Part 1 (BIS, 2002)
5	Frequency of Structure in First Mode, ω_s	1.135 Hz along X-axis and 1.195 Hz along Z-axis
6	Maximum Displacement D_m	Assuming the structure to behave linearly
	(a) At the Base of Water Tank	22 mm along X-axis and 21 mm along Z-axis
	(b) At the Roof Level	16 mm along X-axis and 16 mm along Z-axis
7	Maximum Permissible Displacement D_p	With 25% effectiveness ratio
	(a) At the Base of Water Tank	16.5 mm along X-axis and 15.75 mm along Z-axis
	(b) At the Roof Level	12 mm along X- and Z-axes

2. Structural Analysis

The example structure is analytically modeled and analyzed with the software STAAD PRO, for the inherent structural damping of 5% and for the seismic conditions of Zone III as per the provisions of IS 1893, Part 1 (BIS, 2002), in the following three cases:

- Case 1:** The RC frame alone is supporting the structure and only the gravitational loads are acting under the static condition (as has been the design consideration for most of the ES).
- Case 2:** The masonry walls are contributing as diagonal struts (see Figure 14) along with the RC frames in line with the provisions of the clause 7.10 of IS 1893, Part 1 (BIS, 2002). The dynamic forces due to the earthquake are acting along with the other gravitational loads.
- Case 3:** The RC frame alone is supporting the structure, i.e., the masonry walls are not contributing structurally. The dynamic forces due to the earthquake are acting along with the other gravitational loads.

3. Discussion on Analytical Results

The column stresses obtained from the analysis are normalized with respect to the maximum column stress under Case 1 (in the column A5) and are presented in Table 2. From the comparison of these stresses, it may be observed that under the seismic loading together with the stiffness contribution of the masonry as in Case 2, the designs of only two columns (i.e., A1 and C5) out of the 30 columns are governed by the seismic considerations. This implies that with safety factors already included in the design and the masonry acting as diagonal strut, the structure should be safe under the seismic loading. However, the performance of the masonry-infilled RC frames in the past earthquakes has been with disastrous consequences. This may be attributed to poor quality control of the masonry work. The masonry walls are constructed after the construction of the RC frames and generally are not properly packed at the top, below the RC frame beams, thus causing a lack of confinement and poor integration of the masonry with the RC frame for desirable stress-strain compatibility.

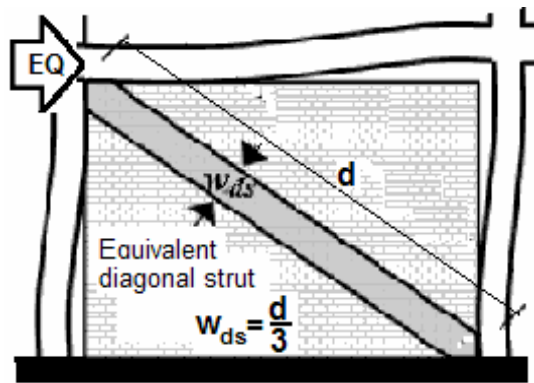


Fig. 14 Stiffness contribution of masonry

Table 2: Maximum Normalized Stress in Columns

Column No.	Maximum Normalized Stress			% Increase over Case 1	
	Case 1	Case 2	Case 3	Case 2	Case 3
A1	0.39	0.44	0.87	11.25	122.24
B1	0.64	0.64	1.14	0.00	79.25
C1	0.67	0.69	1.16	2.12	72.28
A2	0.50	0.50	0.95	0.00	90.98
B2	0.90	0.90	1.39	0.00	53.36
C2	0.75	0.78	1.04	3.37	38.06
A3	0.51	0.51	0.96	0.00	88.42
B3	0.59	0.59	1.18	0.00	100.72
C3	0.69	0.70	1.10	1.29	59.38
A4	0.57	0.58	1.09	3.06	91.54
B4	0.61	0.61	1.24	0.00	102.97
C4	0.68	0.70	1.28	2.74	88.81
A5	<u>1.00</u>	1.01	1.74	1.03	74.08
B5	0.74	0.74	1.26	0.00	69.33
C5	0.65	0.78	1.18	20.30	83.19

In view of the above-mentioned reasons the structural contribution of the masonry is ignored, and the RC frame alone should be considered for structural design as in Case 3. It is evident from the stresses in the columns that in Case 3 the seismic loading is the governing load case for all the columns, and thus the structure is grossly unsafe. Therefore, the existing structures, which have been designed for the Case-1 type conditions, are required to be retrofitted for the Case-3 type conditions. The maximum stress is in the column A5, which is exceeded by 74% under the seismic loading, as compared to the gravity loads only.

4. Retrofitting Strategy

The deformed shape of the existing structure in its first mode of vibration under the seismic loading is shown in Figure 15. The retrofitting is governed by the purpose of reducing the structural deformations from D_m to D_p (i.e., from 16 to 12 mm at the roof level, as shown in Table 1) under the earthquake excitation. This is achieved by incorporating TSWDs in the structure for achieving a higher equivalent damping ratio without any stiffness loss and structural damage for the worst loading combination (i.e., Case 3). The retrofitting design of the ES with TSWDs is based on the following facts and assumptions:

1. The contribution of the superimposed load (LL) to the total load in residential buildings is of the order of 12% (with a possible variation of $\pm 6\%$). By assuming a stiffness variation of $\pm 20\%$ due to the execution and design inconsistencies, the cumulative frequency variation range of the ES is $\pm 12\%$. Thus, the range of detuning is also assumed as $\pm 12\%$.
2. The DMF is maximum at $\beta = 1$. The existing structure is to be retrofitted for this condition. The existing structure is considered as an SDOF system of the first-mode frequency and participating mass. Accordingly, the damper parameters, i.e., frequency and mass ratio, are determined.
3. The TSWDs are located at the points of maximum deformation (i.e., the roof of the structure and the base of the OHT) and are rigidly attached to the structure. The structural deformation at the location of the respective TSWD is the corresponding vibration amplitude (Yalla, 2001).
4. The structure has adequate safety margins (of the order of 50%) under the gravitational loading. The maximum stress due to the earthquake loading is however exceeded by 74%; hence, a response reduction of 25% is considered adequate for bringing the structure within safety limits.

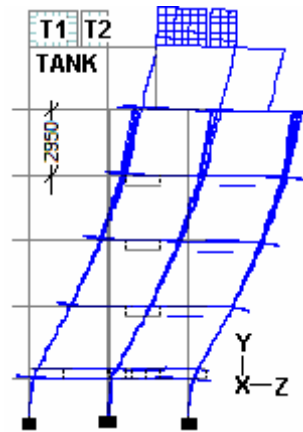


Fig. 15 Deformed shape of existing structure along Z-axis

5. Design of TSWD Retrofitting System

The dynamic properties of the ES are beyond the scope of modification. Hence, the design of a TSWD retrofitting system is limited to the determination of location, geometry and number of TSWDs for the target response reduction. The design procedure is simplified by the use of performance charts (see Figures 11(a)–11(c)). The steps for the retrofitting design of the ES are as given below:

1. The first-mode frequency ω_s , the corresponding participating mass m_s and damping ratio ξ_s , the maximum deformation D_m during the earthquake loading, the maximum permissible deformation D_p during the earthquake after retrofitting, and the target effectiveness ratio E are determined and tabulated as in Table 1.

2. For the structural damping ratio of 5%, the chart of Figure 11(b) is used in determining the mass ratio. For a TSWD of the damping ratio ξ_d of 12% and effectiveness ratio of 25% with 12% detuning, the required mass ratio is obtained as 1.4%. Thus, the total damping mass required is 12,390 kg.
3. Five frequencies of TSWDs (i.e., ω_d) are chosen within $0.88\omega_s - 1.12\omega_s$, with ω_s as the central frequency. The total damping mass is to be equally distributed (i.e., 2,478 kg each) in the 5 designated sizes of TSWDs. The chosen frequencies and corresponding tuning ratios are mentioned in Table 3 (see Columns 2, 3 and 4).
4. The plan dimensions of the TSWD Nt3 for $\omega_d = \omega_s$ are determined from Equations (4) and (5a) for a vibration amplitude of 12 mm (i.e., D_p at the roof level). The variation of tuning ratio with the depth of water is shown in Figure 16. It is observed that after a depth of 250 mm, the effect of depth on sloshing frequency diminishes. Hence, the depth of water in the TSWDs is fixed at 250 mm. The dimensions of all TSWDs are thus determined for the water depth of 250 mm (see Columns 5 and 6 in Table 3).
5. The dimensions of the TSWD Et are determined for a frequency $\omega_d = \omega_s$ and for a vibration amplitude equal to D_p at the tank base level (i.e., 15.75 mm) from Equations (4), (5a) and (5b). The dimensions of the TSWDs are fixed for the water depth of 250 mm (see Column 5 and 6 in the last row of Table 3).
6. The damping ratio for each size of TSWD is determined by taking the mean of the values obtained from Equations (7a) and (7b) (see Columns 7 and 8 in Table 3) with D_p as the amplitude of vibration.
7. The sloshing mass in each size of TSWD is determined from Equation (6) (see Column 9 in Table 3). Accordingly, the number of TSWDs required in each size is determined (see Column 10 in Table 3).

TABLE 3: Properties of Proposed TSWDs

Name Designated	Frequency (Hz)		Tuning Ratio f	Dimension a (mm)		Damping Ratio ξ_d (%)		Sloshing Mass m_d (kg)	No. of TSWDs
	Z	X		Z	X	Z	X		
1	2	3	4	5	6	7	8	9	10
Nt1	1.052	0.999	0.88	630	670	12	11.5	60.2	40
Nt2	1.123	1.067	0.94	570	610	12.9	12.2	47.0	52
Nt3	1.195	1.135	1.0	520	560	13.7	12.7	37.3	64
Nt4	1.267	1.203	1.06	480	510	14.5	13.4	29.4	80
Nt5	1.338	1.271	1.12	430	470	15.6	14.1	22.8	84
Et	1.195	1.135	1	489	559	17.8	15.4	39	28

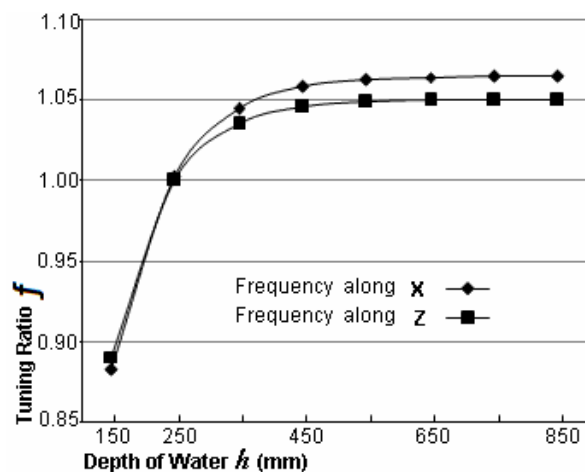


Fig. 16 Variation of tuning ratio with respect to depth of water

6. Performance Check of TSWD Retrofitting System

With the TSWD retrofitting system proposed in Table 3, the total sloshing mass available is 12,598 kg or the mass ratio provided is 1.42%. The magnification factor DMF_0 of the structure without retrofitting for the condition $\beta = 1$ and 5% damping ratio is 10. The magnification factor DMF_r of the retrofitted structure with different first-mode frequencies of the structure, as mentioned in Columns 2 and 3 of Table 3, is evaluated by using Equation (10a). The effectiveness ratio of the retrofitting system for each frequency is then determined from Equations (12a) and (12b) and plotted in Figure 17. The cumulative approximation in the frequency assessment of the example structure is $\pm 12\%$ and it may be observed that for the frequency range of $0.88\omega_s - 1.12\omega_s$, an effectiveness ratio in excess of 29% is achievable with the mass ratio of 1.42%.

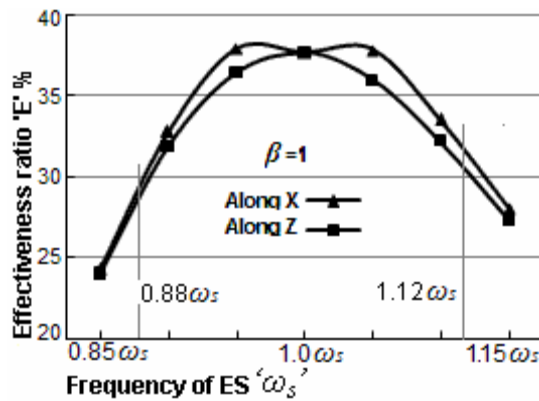


Fig. 17 Performance of multiple-TSWDs system

The proposed retrofitting regime may be considered adequate for the 25% structural response reduction under a dynamic loading. Thus, the maximum roof displacement may be restricted within the permissible limit for the first-mode frequency. The frequency of each TSWD will be different due to the variation in vibration amplitude, depending on the structural deformation at its location. However, the cumulative effect of all the TSWDs as a system will be similar to that presented in Figure 17.

7. Execution Scheme of TSWD Retrofitting System

The additional TSWDs (i.e., Nt1 to Nt5) may be fabricated from G.I. sheets in clusters. A total of 320 additional TSWDs in four clusters of 80 each are provided on the roof in two tiers, as shown in Figures 18(a) and 18(b).

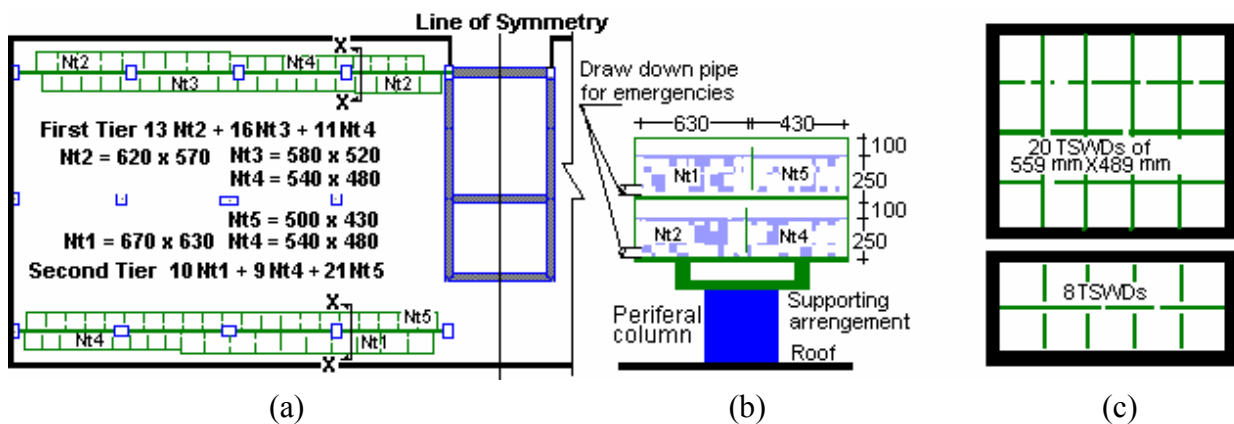


Fig. 18 Execution scheme of TSWD retrofitting system: (a) Placement of TSWDs ‘Nt’ at roof level; (b) Section X-X, (c) OHT modified as TSWD ‘Et’

The existing OHT is modified only in plan for making the TSWDs designated as Et, by inserting the 1-mm thin GI or acrylic sheet vertical partitions. There are two overhead tanks of 2.8×1.96 m (designated

as T1) for the potable use and 2.8×0.98 m (designated as T2) for the flushing use, respectively. These tanks are divided in the TSWDs of 559×489 mm dimensions as shown in Figure 18(c). The drawdown pipe should be fixed above the threshold depth of 250 mm from the bottom of OHT. The sloshing mass of water in each TSWD designated as E_t is 39 kg, thus making a total of 1,092 kg mass in 28 such TSWDs.

The internal partition walls between the TSWDs are to be kept 25 mm short from the top sheet to allow for the spillage due to sloshing, if any. All the TSWDs of one cluster are interconnected through holes at the bottom of the vertical partitions. The holes in the bottom serve as the auto-levelers of the water mass in a TSWD cluster.

The overall depth of the proposed retrofitting system is less than 1,000 mm (i.e., the parapet height) above the finished roof level. The new TSWDs (i.e., Nt1 to Nt5) are accommodated along the parapet in such a way that the weight of the TSWDs is directly transferred to the peripheral columns and major part of the roof remains available for the occupancy use. The increase in the total mass of the example structure due to the provision of additional TSWDs may be compensated by replacing the masonry parapet with MS pipe railings. This proposal accomplishes the retrofitting of the example structure without any architectural, structural or occupancy interference.

PERFORMANCE OF RETROFITTED STRUCTURE DURING EARTHQUAKES

For an unretrofitted structure of 5% damping ratio, the 29% effectiveness ratio for the retrofitting system translates into an effective structural damping ratio of 7% (refer Equations (11), (12a) and (12b)). Thus, an existing structure having an inherent damping of 5% may be considered to have achieved an effective damping of 7% after retrofitting, without any loss of stiffness.

The performances of the existing and retrofitted structures are evaluated with respect to the recorded ground motions of the El Centro 1940 earthquake, as in Chopra (1995), for different orientations of the structure and are presented in Figure 19. The maximum structural displacement of 17.6 mm of the unretrofitted structure is anticipated with its X-axis parallel to the east-west component of the ground motion. After retrofitting, this is reduced to 14.2 mm (i.e., the response reduction is 19%). The minimum structural displacement of 14.9 mm of the unretrofitted structure is anticipated with its Z-axis parallel to the north-south component of the ground motion. After retrofitting, this is reduced to 12.5 mm (i.e., the response reduction is 15%). Thus, after retrofitting, a response reduction ranging from 15% to 19%, depending on the orientation of the structure with respect to the ground motion, is predicted. Further, since the relation between mass ratio and effectiveness ratio is nearly linear, a higher effectiveness may be achieved by increasing the mass ratio.

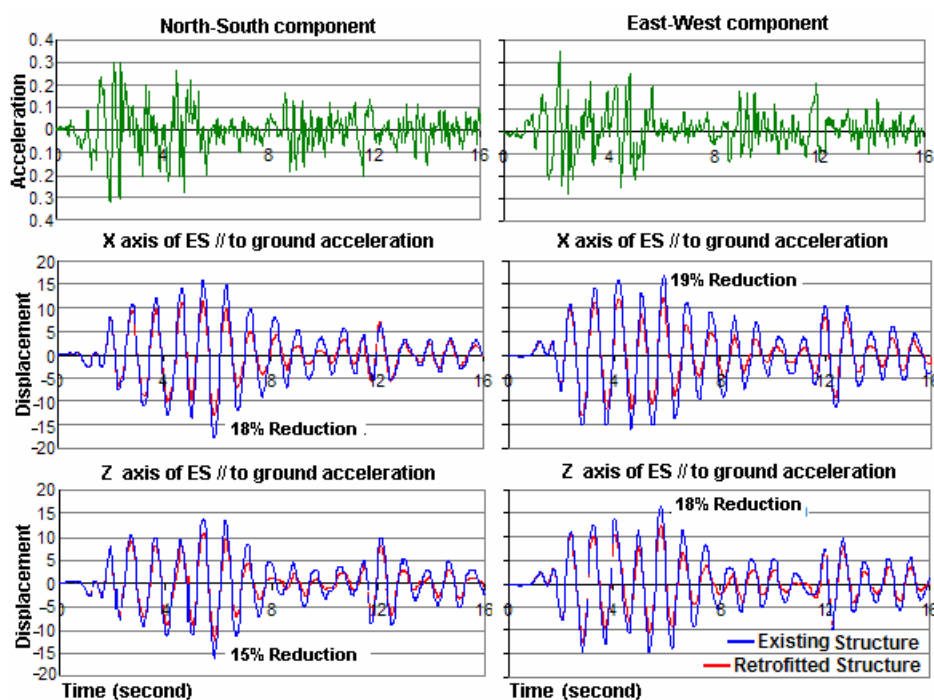


Fig. 19 Response of retrofitted structure against El Centro ground motion

CONCLUDING REMARKS

The proposed retrofitting system will ensure a more predictable performance of the masonry-infilled RC structure during an earthquake, as the effective damping ratio increases without any stiffness loss. The maximum response of the structure after retrofitting is reduced globally. This effect will be more pronounced for the ES with low damping ratios, as is evident from Figure 11(a). There exists an almost linear relation between effectiveness ratio and mass ratio; hence, the performance of the TSWD system may further be improved by increasing the mass ratio. A sloshing mass equivalent to the 0.12% mass ratio is readily available in the OHT for utilization as TSWD with nominal effort and cost.

The multiple TSWDs are effective for a complete range of practically possible frequencies and are feasible for all the existing structures of medium heights. The term, effectiveness ratio E , for the retrofitting system has been introduced to measure its performance numerically in an abstract form. The design charts have also been developed for the real-life structural ranges, in order to reduce the computation effort. TSWDs require a negligible trigger level due to the absence of mechanical friction as compared to TMDs. The retrofitting effect of TSWDs comes into action with the start of the sloshing, as initiated by the structural deformations. The rectangular TSWDs can be designed in conformity with the principal axes of the ES, thus offering functionality in all the possible directions in the horizontal plane.

The above-described regime provides an all-time sustainable preparedness against the earthquakes without any maintenance cost. The non-interfering nature of this retrofitting system is the most attractive feature for adoptability and application. The proposed system is very useful for the scattered and remotely placed but important installations that are sensitive to the vibratory loads. This system does not have any adverse effects on the existing structure to be retrofitted. The purpose of this paper was to illustrate the applicability of multiple TSWDs for existing structures with the use of simple design methodology and ease of installation. Furthermore, the TSWDs may be integrated with the plumbing system of the building and utilized against the fire hazard and water distress conditions.

REFERENCES

1. Abramson, H.N. (editor) (1966). "The Dynamic Behavior of Liquids in Moving Containers, with Applications to Space Vehicle Technology", Report NASA SP-106 Prepared by the Southwest Research Institute, National Aeronautics and Space Administration, Washington, DC, U.S.A.
2. BIS (2000). "IS 456: 2000—Indian Standard Plain and Reinforced Concrete—Code of Practice (Fourth Revision)", Bureau of Indian Standards, New Delhi.
3. BIS (2002). "IS 1893 (Part 1): 2002—Indian Standard Criteria for Earthquake Resistant Design of Structures, Part 1: General Provisions and Buildings (Fifth Revision)", Bureau of Indian Standards, New Delhi.
4. Chey, M.H., Carr, A.J., Chase, J.G. and Mander, J.B. (2008). "Resetable Tuned Mass Damper and Its Application to Isolated Stories Building System", Proceedings of the 14th World Conference on Earthquake Engineering, Beijing, China (on CD).
5. Chopra, A.K. (1995). "Dynamics of Structures: Theory and Applications to Earthquake Engineering", Prentice-Hall, Inc., Englewood Cliffs, U.S.A.
6. Den Hartog, J.P. (1956). "Mechanical Vibrations", McGraw-Hill, New York, U.S.A.
7. EERI (2001). "Learning from Earthquakes: Preliminary Observations on the Origin and Effects of the January 26, 2001 Bhuj (Gujarat, India) Earthquake", EERI Special Earthquake Report, Earthquake Engineering Research Institute, Oakland, U.S.A.
8. Frahm, H.H. (1911). "Results of Trials of the Anti-rolling Tanks at Sea", Journal of the American Society for Naval Engineers, Vol. 23, No. 2, pp. 571–597.
9. Fujino, Y., Pacheco, B.M., Chaiseri, P. and Sun, L.M. (1988). "Parametric Studies on Tuned Liquid Damper (TLD) Using Circular Containers by Free-Oscillation Experiments", Structural Engineering/Earthquake Engineering, JSCE, Vol. 5, No. 2, pp. 381s–391s.
10. Graham, E.W. and Rodriguez, A.M. (1952). "The Characteristics of Fuel Motion Which Affect Airplane Dynamics", Journal of Applied Mechanics, ASME, Vol. 19, No. 3, pp. 381–388.

11. Hemalatha, G. and Jaya, K.P. (2008). "Water Tank as Passive TMD for Seismically Excited Structures", *Asian Journal of Civil Engineering (Building and Housing)*, Vol. 9, No. 4, pp. 349–366.
12. Jaiswal, O.R. (2004). "Simple Tuned Mass Damper to Control Seismic Response of Elevated Tanks", *Proceedings of the 13th World Conference on Earthquake Engineering*, Vancouver, Canada, Paper No. 2923 (on CD).
13. Kareem, A. and Kline, S. (1995). "Performance of Multiple Mass Dampers under Random Loading", *Journal of Structural Engineering*, ASCE, Vol. 121, No. 2, pp. 348–361.
14. Kourakis, I. (2007). "Structural Systems and Tuned Mass Dampers of Super-Tall Buildings: Case Study of Taipei 101", M.Eng. Thesis, Department of Civil and Environmental Engineering, Massachusetts Institute of Technology, Cambridge, U.S.A.
15. Lieping, Y., Xinzhen, L., Zhe, Q. and Jianqun, H. (2008). "Distributed TLDs in RC Floors and Their Vibration Reduction Efficiency", *Earthquake Engineering and Engineering Vibration*, Vol. 7, No. 1, pp. 107–112.
16. Makino, A. (2009). "High-Rise Building Seismic Vibration Control Using Large Tuned Top-Floor Mass Damper", *Journal of Disaster Research*, Vol. 4, No. 3, pp. 246–252.
17. Modi, V.J. and Welt, F. (1987). "Vibration Control Using Nutation Dampers", *Proceedings of the International Conference on Flow Induced Vibrations*, Bowness-on-Windermere, U.K., pp. 369–376.
18. Nawrotzki, P. (2005). "Visco-elastic Devices for the Seismic Control of Machinery, Equipment and Buildings", *Proceedings of the 9th World Seminar on Seismic Isolation, Energy Dissipation and Active Vibration Control of Structures*, Kobe, Japan (on CD).
19. Rai, N.K., Reddy, G.R., Ramanujam, S., Venkatraj, V. and Agrawal, P. (2009). "Seismic Response Control Systems for Structures", *Defence Science Journal*, Vol. 59, No. 3, pp. 239–251.
20. Rai, N.K., Reddy, G.R. and Venkatraj, V. (2010). "Seismic Retrofitting of Existing Structures: Over Head Tank as TSWD", *Proceedings of the 14th Symposium on Earthquake Engineering*, Roorkee, Vol. 2, pp. 1294–1305.
21. Reddy, G.R., Parulekar, Y.M., Dubey, P.N., Sharma, A., Vaity, K.N., Ravi Kiran, A., Agrawal, M.K., Vaze, K.K., Ghosh, A.K. and Kushwaha, H.S. (2008). "Studies on Response of Structures, Equipment and Piping Systems to Earthquake and Its Mitigation", *BARC Newsletter*, No. 290, pp. 15–30.
22. Tamura, Y., Fujii, K., Ohtsuki, T., Wakahara, T. and Kohsaka, R. (1995). "Effectiveness of Tuned Liquid Dampers under Wind Excitation", *Engineering Structures*, Vol. 17, No. 9, pp. 609–621.
23. Tsai, H.-C. and Lin, G.-C. (1993). "Optimum Tuned-Mass Dampers for Minimizing Steady-State Response of Support-Excited and Damped Systems", *Earthquake Engineering & Structural Dynamics*, Vol. 22, No. 11, pp. 957–973.
24. Vandiver, J.K. and Mitome, S. (1979). "Effect of Liquid Storage Tanks on the Dynamic Response of Offshore Platforms", *Applied Ocean Research*, Vol. 1, No. 2, pp. 67–74.
25. Villaverde, R. (2000). "Implementation Study of Aseismic Roof Isolation System in 13-Story Building", *Journal of Seismology and Earthquake Engineering*, Vol. 2, No. 2, pp. 17–27.
26. Yalla, S.K. (2001). "Liquid Dampers for Mitigation of Structural Response: Theoretical Development and Experimental Validation", Ph.D. Dissertation, Department of Civil Engineering and Geological Sciences, University of Notre Dame, Notre Dame, U.S.A.
27. Yu, J.-K., Wakahara, T. and Reed, D.A. (1999). "A Non-linear Numerical Model of the Tuned Liquid Damper", *Earthquake Engineering & Structural Dynamics*, Vol. 28, No. 6, pp. 671–686.